FEATURE ARTICLE

Integrated Multifunctional Nanosystems for Medical Diagnosis and Treatment

By *Donglu Shi**

This article provides an overview on the development of integrated multifunctional nanosystems for medical diagnosis and treatment. In particular, a novel system is developed specifically for achieving simultaneous diagnosis and treatment of cancer. Critical issues are addressed on the architecture and assembly of nanocomponents based on medical requirements: targeted in vivo imaging, controlled drug release, localized hyperthermia, and toxicity. Nanotube-based carriers are summarized with surface functionalized properties. Other types of nanocarriers are also included such as super paramagnetic composite nanospheres and biodegradable hydroxylapatite nanoparticles. In addition, polymeric-based nanosystems are introduced with several novel features: they can be bio-dissolved due to environmental pH and temperature fluctuations. The nanocarriers are surface tailored with key functionalities: surface antibodies for cell targeting, anti-cancer drug loading, and magnetic nanoparticles for both hyperthermia and MRI. Future requirements, aims, and trends in the development of multifunctional nanosystems, particularly with intelligent functionalities for fundamental studies, are also provided.

1. Introduction

There has been an increasing need for the early detection of cancer, prior to the detection of anatomic anomalies, in order to obtain maximum therapeutic benefit. In early diagnosis, the current clinical magnetic resonance imaging (MRI) scan can readily detect lesions as small as a few millimeters.[1–6] Dynamic MRI of human cancer in mice has reached a high spatial resolution.[7,8] But MRI is costly and time consuming to implement. Furthermore, in clinical diagnosis with MRI, it is difficult to achieve simultaneously high spatial and temporal resolution. Compared to MRI, optical imaging is much easy to use and cost effective, and can be applied to cancer diagnosis with high resolution in a rapid fashion. Recently, for diagnosing breast cancer, MRI and near-infrared optics have been combined as a potentially more accurate method.[9] By combining these two techniques, MRI produces the basic image of the breast, while simultaneously the near-infrared optical means provides the functional information of the tissue, such as the oxygen consumption rate at a particular region, which could indicate early cancer development.

On the other hand, as a result of diagnosis and surgery being clinically separated procedures, it is difficult to visually locate these small lesions during operation because the cancer cells are not bioluminescent. Furthermore, MRI contrast agents have no cell targeting functions (e.g., they are not specific to tumors), making the interpretation of the diagnosis results largely dependent on the experience of the physician. This leaves an uncertainty in providing a conclusive diagnosis. Therefore, it is highly desirable to develop novel methods that can achieve simultaneous cell targeted in vivo imaging and treatment based on nanotechnology. For instance, ideally, while achieving concurrent high spatial and temporal resolution of the lesions via cell targeting, special non-evasive treatments are implemented by various means, such as localized drug release and hyperthermia, in a controlled fashion.

To achieve simultaneous targeted imaging and treatment, or in vivo imaging-aided surgery, the critical challenges have been the development of multifunctional nanosystems with integrated capabilities. Such a nanosystem must be able to locally biomark cancer cells for efficient therapeutic treatment through a process called "cell targeting."[10–15] In this process, the nanosystem with multifunctionalities, in the nanoparticle form, will be intravenously (i.v.) injected into the blood stream at a very low dosage. Since these nanoparticles are surface functionalized with antibodies that are cancer specific, they will selectively attach onto the cancer cells (they act as the so-called biomarkers or tags). The cell targeting is accomplished based on the antibody–antigen reaction, that is, it is tumor specific.

Localized delivery of drugs into tumor lesions is also a key challenge for successful management of cancers. If designed correctly, one may achieve localized drug release in a highly controlled fashion. The controllability implies an externally installed wireless switch that can turn on and off the drug release process in the vicinity of the tumor. Nanoparticles with special structures and geometries may offer unique drug delivery capabilities.[16–21] These include hollow nanospheres, nanocapsules, and porous matrix

[*] Prof. D. Shi
Department of Chemical and Materials Engineering
University of Cincinnati
Cincinnati, OH 45221 (USA)
and
The Institute for Advanced Materials and Nano Biomedicine
Tongji University
Shanghai 200092 (China)
E-mail: shid@email.uc.edu

DOI: 10.1002/adfm.200901539

systems through which the drug is dispersed. In drug storage, the drug needs to be protected by the nanostructures from being leaked during the transport process. This will ensure maximum localized drug delivery at the cancer tumor site. In the vesicle-like nanostructures, the drug must be confined to an aqueous or oily cavity protected by a biodegradable membrane.

Suppression of cancer cells can also be accomplished by magnetic hyperthermia without drugs. Magnetic hyperthermia is associated with a heating phenomenon when magnetic nanoparticles such as Fe_3O_4 are placed in an alternating magnetic field.[22–26] The magnetic hyperthermia mechanisms can be explained by both hysteresis and relaxation losses, depending up on the characteristics of the nanomaterials.[22] For ferromagnetic nanoparticles, hysteresis loss counts for the area of the magnetization hysteresis curve. For nanoparticles that exhibit super paramagnetic properties, the so-called Neél relaxation becomes responsible due to fluctuation of the magnetic moment direction across an anisotropy barrier.[22,27] If the nanocarriers are rendered magnetic, hyperthermia can be applied for cancer treatment. Upon arrival of the nanoparticles at the cancer sites via cell targeting, they will heat up locally to 41 °C due to an externally applied alternating magnetic field.[28,29] Above this temperature, the cancer cells can be effectively killed. The hyperthermia treatment does not involve any medicine, but only generates local heat at the cancer regions in a controlled fashion.

Having established the concepts of cell targeting and localized treatment based on nanotechnology, we are able to provide another important aspect in cancer diagnosis from the imaging perspective. For the diagnosis and treatment of cancer, it is highly preferred for the physicians to be able to observe the nanocarriers at all times in a clinically convenient fashion. This will require the nanoparticles, by using the commercial in vivo imaging systems, to be observable through strong fluorescence in deep tissues. This is an important step in simultaneous diagnosis and treatment as the process can noninvasively take place at very early stage of cancer growth.

Therefore, the terminology used in this paper: ''integrated multifunctionality'' specifically implies that the nanosystem is equipped with the following capabilities: cell targeting, drug storage, hyperthermia, and in vivo imaging. This means that the delivered nanocarriers are not only surface functionalized with antibodies that enable them to be targeted at the cancer cells, but also stored with drugs or rendered magnetic for hyperthermia treatment. In addition, fluorescent materials are conjugated on these nanocarriers so that diagnosis and treatment may be carried out simultaneously.

2. Development of Integrated Multifunctional Nanosystems

Based on these biomedical requirements of the nanostructures described, the integrated multifunctional nanosystems for both cancer diagnosis and treatment have been designed and developed as shown in Figure 1. As discussed above, the geometry of the nanocarrier may have some biomedical preferences for both drug storage and fluid dynamics. A hollow or porous structure may be needed for storage and diffuse of drugs. An idealized ''football'' shape has been proposed for the optimum fluid dynamical properties. As shown in Figure 1, the interior of the nanocarrier is filled with anti-cancer drug, which is also attached on the spring-like connections on the outer surface. The spring-like connectors on the outer surface are able to release the drug at their tips upon environmental fluctuations in temperature and pH values. The outer surface of the nanocarrier is conjugated with fluorescent and magnetic nanoparticles for imaging and hyperthermia. Photodynamic chemical sensitizers can also be attached on the surface for photo driven functions in treatment of cancer. The football-shaped shell may dissolve due to temperature changes that are controlled externally, thus releasing the drugs.

The nanosystem depicted in Figure 1 for simultaneous in vivo imaging and treatment will need novel design and development involving multiple components. For imaging purposes, fluorescent materials must be incorporated into the nanosystems while possessing other functionalities such as drug storage, hyperthermia, and targeting. This requires the fluorescent component not only retain its intrinsic properties, such as emissions at the optically preferred range, but should not interfere with the properties of other components. This has been one of the key challenges in the development of multifunctional nanosystems. For instance, in previous studies, it has been found that

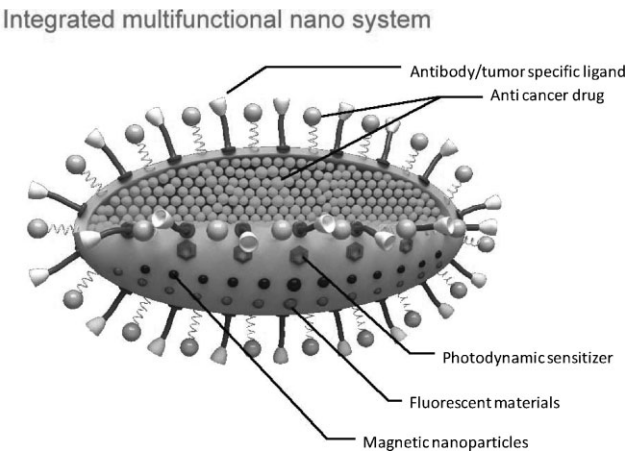

Figure 1. Schematic diagram showing an idealized integrated multifunctional nanosystem to be used in cancer diagnosis and treatment.

Donglu Shi received his Ph. D. in 1986 from the University of Massachusetts at Amherst. After graduation, he took a Scientist position at Argonne National Laboratory in 1988. In 1995, he joined the faculty of the Department of Materials Science and Engineering at the University of Cincinnati. He has edited eight books in nanomaterials, nanomedicine, thin film deposition, biomaterials, medical devices, and superconductivity. He is currently the Editor-in-Chief of *Nano Life*, and the Associate Editor of *Materials Science & Engineering: C*.

conjugation of quantum dots (QDs) onto various nanocarriers such as carbon nanotubes (CNTs) and Fe_3O_4 magnetic nanospheres (MNSs) have resulted in considerable emission blue-shifting.[30]

According to the design shown in Figure 1, the nanocarriers must be rendered fluorescent, emitting visible light, preferably in the near infrared range. For tumor diagnosis, the fluorescent signals must have strong intensities against the background autofluorescence from the animal bodies. This is particularly important for deep tissue imaging. Therefore, the first task in nanotechnology for medical diagnosis is to deposit fluorescent materials onto the nanocarriers. The deposited fluorescent materials must be able to retain their intrinsic optical properties that satisfy all diagnostic requirements. In the following, several unique synthesis methods are introduced for deposition and conjugation of different fluorescent materials on a variety of nanosubstrates including CNTs and Fe_3O_4 nanocomposites.

2.1. Rare Earth Doped Nanophosphors on Multiwalled Carbon Nanotubes (MWCNTs)

What has been described above and depicted in Figure 1 is an idealized design and nanostructure. In reality, the experimental approach has to rely on the identification of suitable and available nanosubstrates that can be of the closest approximations to the model shown in Figure 1. Therefore, for medical diagnosis and treatment, the design and selection of a clinically viable substrate is the key to the development of multifunctional nanosystems. As described in the introduction, an optimized hollow structure may serve as a ''reservoir'' for storage of anti-cancer drugs. The CNT may be qualified as a possible candidate due to its unique properties, including appropriate dimensionality and chemical stability. MWCNTs have hollow structures with inner diameters on the order of 50–150 nm, which may be an appropriate geometry for drug transport and delivery. On the other hand, the CNT structure is thermally stable to high temperatures, which allows surface modifications by a variety of chemical and physical synthesis methods.[31–36]

However, CNTs have been observed to exhibit weak IR emissions,[33,37] and therefore do not have sufficient fluorescence for in vivo imaging. Among all fluorescent materials, those containing optically active rare earth ions have been of great interest in both fundamental studies and biomedical applications. Their unexpected optical properties have been found to be dependent on electron–phonon interaction strength, on particle size,[38,39] surface quenching,[40] modification in transition intensity and fluorescence lifetime,[41] single ion luminescence,[42] and restricted phonon relaxation and anomalous thermalization.[43–47] All these behaviors are related to structural characteristics of the nanoparticles and distribution of the emission centers within them.

Based on these considerations, a more realistic design of the nanosystem is developed, and is shown in Figure 2. In this design, as an initial step, experiments have been carried out to deposit rare earth doped Y_2O_3 on MWCNTs.[36] These MWCNTs were 70–150 nm in diameter and several microns in length. The rare earth doped Y_2O_3 was deposited on MWCNTs by a solution method[37]

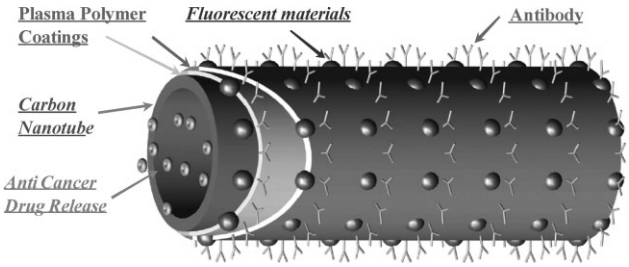

Figure 2. Schematic diagram illustrating the concept of a CNT functionalized with plasma polymer coating, luminescent QDs, and loaded with anti-cancer drugs. The functionalized CNT can be used as a biomarker and a drug carrier.

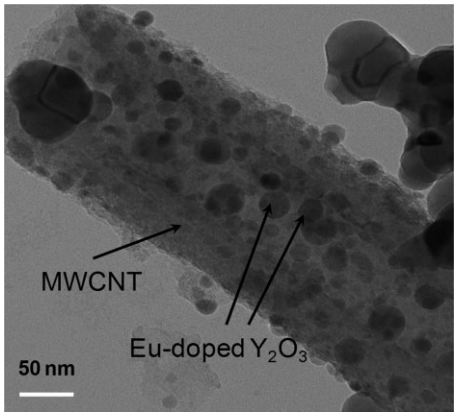

Figure 3. Bright-field TEM image showing the surface deposition of Eu-doped Y_2O_3 film on a MWCNT, heat treated at 950 °C. The darker nanoparticles on MWCNT are the crystalline Eu-doped Y_2O_3.

and heat treated for consolidation at 650 and 950 °C, respectively. Figure 3 shows a bright-field transmission electron microscopy (TEM) image of a surface-functionalized MWCNT heat treated at 950 °C. As seen in this figure, the outer surface of the nanotube is uniformly coated by nanoparticles of rare earth doped Y_2O_3. In the selected area electron diffraction study, it has been found that the diffuse diffraction pattern acquired from the tubular substrate corresponds to the (002) graphite layer of the CNTs. The diffraction patterns from the surface-coated nanoparticles can be indexed using the structural data of Y_2O_3 crystals described by hexagonal unit cell. This result is also confirmed by the corresponding Fourier-filtered transformed (FFT) image that is indexed from the same Y_2O_3 structure. The energy-dispersive X-ray spectroscopy (EDS) measurements indicate the major elements of carbon, yttrium, and europium on the nanotube surface, which are consistent with the coating process and TEM observations. The above results suggest the identity of the nanoparticle as Eu-doped Y_2O_3.

Under 355-nm pulsed laser excitation, Eu^{3+} luminescence has been observed at room temperature from samples of the coated MWCNTs heat-treated at 650 and 950 °C (Fig. 4). As shown in Figure 4a and b, the emission lines are characteristic of the Eu^{3+} $^5D_0$–^7F_J ($J = 0, 1, 2$) electronic transitions. The efficiency of luminescence emission from the sample treated at 950 °C is much higher than that from the sample treated at 650 °C. The sharp lines

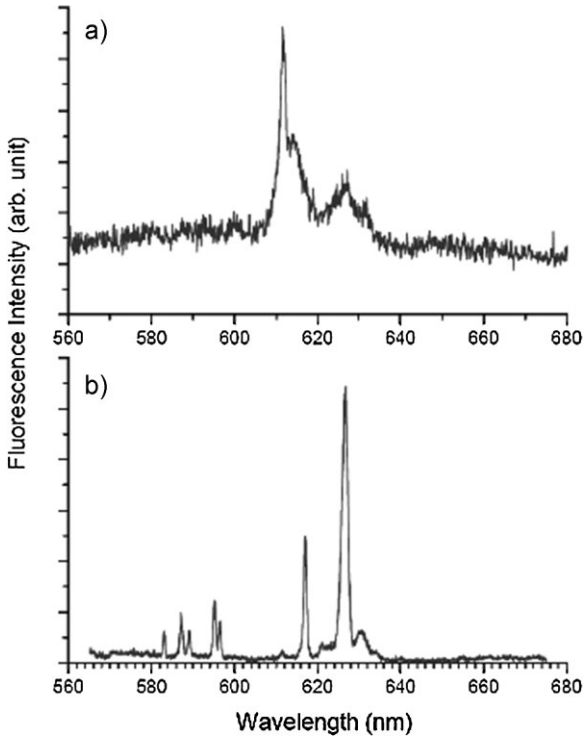

Figure 4. Luminescence emission spectra of Eu-doped Y_2O_3-coated MWCNTs a) heat treated at 650 °C and b) at 950 °C. Reproduced with permission from Reference [36], copyright 2006 Wiley-VCH.

in the emission spectrum of the sample treated at 950 °C indicate that Eu^{3+} doped in Y_2O_3 has a well-defined crystalline structure, whereas the broader spectrum of the sample treated at 650 °C suggests a more disordered atomic-scale structure.

The above results have shown that fluorescent materials can be deposited onto CNTs while retaining their optical properties. It is, therefore, possible to design and synthesize other types of fluorescent materials on nanosubstrates for medical diagnosis.

2.2. Deposition of Fluorescent Materials on Biodegradable Nanocarriers

In search of nanocarriers for medical diagnosis and therapy, one of the concerns has been their biodegradability and toxicity.[48–53] It is desired that these nanocarriers, after diagnosis and treatment procedure, be removed from the body through natural biological processes in a medically safe fashion. However, some of the nanomaterials, although exhibiting fascinating properties for medical applications, may present some toxic effects.[48] It is, therefore, important to search for nontoxic and biocompatible substrates in biomarking and drug-delivery applications.[10–21] The difficulty involved in choosing a good nanocarrier candidate has been the paradox that a highly biodegradable material may not be fluorescent. Thus, it becomes essential to develop novel approaches that can integrate needed properties in one system. The design concepts depicted in Figures 1 and 2 illustrate the ideal structures one is able to accomplish through nanotechnologies.

Based on the initial experimental results presented in Section 2.1, it is possible to deposit fluorescent materials on biodegradable nanosubstrates. In the calcium phosphate system, hydroxyapatite (HA) $[Ca_{10}(PO_4)_6(OH)_2]$ exhibits superb biological stability and affinity.[54–59] HA has been routinely used in orthopedic surgery in both powder and bulk forms.[60] Due to its biodegradable nature, HA nanoparticles may serve as an ideal candidate for both cancer diagnosis and drug delivery. It has been reported that the surface of HA is quite porous, an ideal structure for drug storage.[61]

Taking advantage of HA's biodegradability, based on the thermal deposition experimental results presented in Section 2.1, HA nanoparticles have been surface functionalized by depositing optically active Y_2O_3:Eu^{3+} nanoparticles, leading to strong visible luminescence. It should be noted that Y_2O_3 ceramic has been used as substrate in orthopedic implants as a bioinner material.[62] Furthermore, the Eu doping level is considered extremely low and may have minimum toxic effects. It has been found that the microstructure of rare earth nanophosphor–HA composites and their optical properties can be well controlled by varying the annealing temperature. The Eu^{3+}-doped Y_2O_3 on HA exhibits luminescent emission in the visible light range, and the phosphors are associated with doped HA nanoparticles via Y_2O_3 as the medium. The biodegradable nature of HA, combined with optically active rare earth doped phosphor nanoparticles may find important applications as a transport agent in biomedical systems.

Several nanomaterials have been found to exhibit visible and infrared emissions, but their intensities are often too low for in vivo imaging.[63–66] For instance, single walled CNTs have been known to have emissions in the infrared range, but their weak intensity means that they are unsuitable for deep tissue and whole-body in vivo imaging.[63,64] Fluorescent proteins and small organic dyes have been used as fluorescent contrast agents for living animal imaging.[67–72] The ideal fluorescent probe would contain a fluorescent agent that emits light on target emission.

Among all fluorescent nanomaterials, QDs have superior properties, including higher quantum yield and much sharper emission spectra. QDs can be "tuned" based on their size and have superb optical properties, resulting from quantum confinement effects.[73,74] They offer high resistance to photobleaching, thus making them attractive materials for optoelectronics[75,76] and in vivo biosensing applications.[77] Bruchez et al.[78] and Chan and Nie[77] first reported the use of QD conjugates for labeling biological specimens. Subsequently, several other studies demonstrated the labeling of whole cells and tissue sections using different surface modifications of QDs.[79–81] Due to these unique properties, extensive research has also been carried out on cancer diagnosis by using QDs.[82–87] The first study of QD for cell labeling was reported by Chan and Nie in 1998.[77] In our previous research, we have demonstrated that it is possible to use HA nanoparticles, one of the well-known biodegradable materials, for clinical in vivo applications.[88,89] However, in order to diagnose deep-tissue cancer cells under whole-body in vivo imaging conditions, much brighter luminescent nanoparticles are needed, particularly for complex tissue structures.

For achieving deep tissue imaging in vivo, HA nanoparticles have been surface conjugated with QDs (HA–QD). To obtain the HA–QD conjugation, a unique coupling procedure has been employed. Figure 5 shows a bright-field TEM image of the HA–

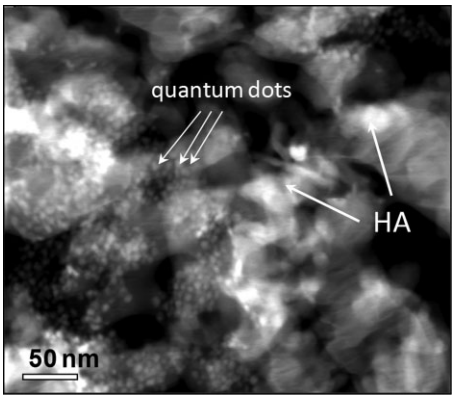

Figure 5. Bright-field TEM showing the image of QDs attached on the HA nanoparticles surface; the finer particles are QDs dispersed on the HA substrate (gray and larger particles in the background), as identified by both HRTEM and EDX.

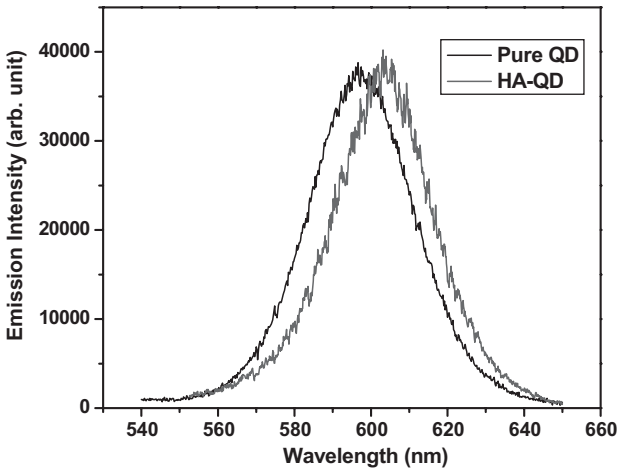

Figure 6. Typical emission spectrum of pure EviTags 600 CdSe/ZnS QDs without coupling–the maximum peak is at 600 nm with line width of 13 nm–and luminescence spectrum of QD attached on HA nanoparticles. The experimental curve is fit by a Lorentzian line shape function with peak centered at 603 nm and line width of 32 nm. Reproduced with permission from Reference [89], copyright 2008 the Institute of Physics.

QD. As can be seen, the QDs have a quite uniform size distribution in the range between 5 nm and 10 nm. The QDs exhibit a distinctive morphology that can be easily differentiated from the substrate HA nanoparticles, whose dimensions (~50 nm) are considerably larger than those of the QDs. High-resolution TEM (HRTEM) images clearly show the lattice structure of CdSe/ZnS QDs deposited on the surfaces of the HA nanoparticles.[88,89] To further identify the conjugation of QDs on the HA nanoparticles' surfaces, the energy dispersive X-ray spectrum (EDX) has also been acquired, confirming the elemental signals from the CdSe/ZnS QDs and HA.[88,89]

Figure 6 shows the emission spectrum of CdSe/ZnS QDs adsorbed on the HA nanoparticles. The spectrum is obtained with laser excitation at 355 nm at room temperature. The luminescence spectrum is centered at 603 nm, a 3-nm redshift from the EviTags 600 CdSe/ZnS QDs. In comparison with 13-nm linewidth for the single QD, the 32-nm linewidth for the studied system is broadened as a result of conjugation with HA nanoparticles. Because the emission wavelength of the individual QD is a function of size and local environment, the observed line broadening can be understood as index of variation in local environment.

2.3. Conjugation of Quantum Dots on Carbon Nanotubes

The development of an ideal nanostructure with all integrated properties for clinical diagnosis is still a great challenge in both materials and medical sciences. One of the challenges lies in creating optimum emission intensity and frequency from the nanocarriers, that provides the highest possible resolution in a three-dimensional fashion in deep-tissue in vivo imaging. In particular, deep-tissue tumor imaging requires a frequency close to the near-infrared range (>700 nm) for avoiding the background emissions from the animal body autofluorescence. CNTs are intrinsically florescent in the near-infrared region,[63,64] whereas human tissues and biological fluids[83] are practically transparent to these emissions.[84–87] However, these emission intensities are quite low and not useful for deep-tissue or live-animal imaging.

It has been found that, for in vivo imaging, QDs must have adequate circulating lifetime, must show minimal nonspecific deposition, and must retain their fluorescence for sufficiently long periods. This nonspecific targeting can be reduced by coating nanoparticles with hydrophilic polymers, such as polyethylene glycol (PEG), to allow greater vascular circulation time, but nonspecific uptake cannot be eliminated completely.[90–92]

Toxicity and biocompatibility have been major concerns for the use of nanoparticles in biomedical applications.[93,94] Before clinical applications of QDs become possible, the biocompatibility of these nanoparticles must also be thoroughly investigated. For cell culture studies, a biocompatible particle must be nontoxic and inert, as well as stable over the course of an assay. Recently, Derfus et al.[95] used cultured liver cells to determine the cytotoxicity of CdSe/ZnS QDs with various surface coatings. The results suggested that the surface coatings must be sufficiently stable in order to prevent oxidation of the QD surfaces, which results in the release of divalent cadmium, a known toxin and suspected carcinogen. PEG and other biologically inert polymers may be useful for making QDs biocompatible. So far, nearly all studies on the in vivo use of QDs have reported normal organism development and no short-term detectable toxicity.[80,96–99]

To explore further on the integration of multifunctional nanosystems, we have carried out experiments on conjugating QDs on CNTs. The CNTs have been surface functionalized by a unique plasma polymerization process.[100–103] The procedure for coupling the acrylic acid (AA)-functionalized CNTs with amine-functionalized QDs has been reported previously. Two different QDs have been used for CNT conjugation, with 680- and 800-nm emissions, respectively. QDs with emission wavelength of 680 and 800 nm are supplied by Invitrogen Corporation (Carlsbad, CA, USA). This QD has a core of CdSeTe and a shell of ZnS with a covalently attached, amine-functionalized layer of PEG.

TEM images of CNTs and CNTs with surface conjugated QD_{680} (QD with emission at 680 nm) are shown in Figure 7. Figure 7a

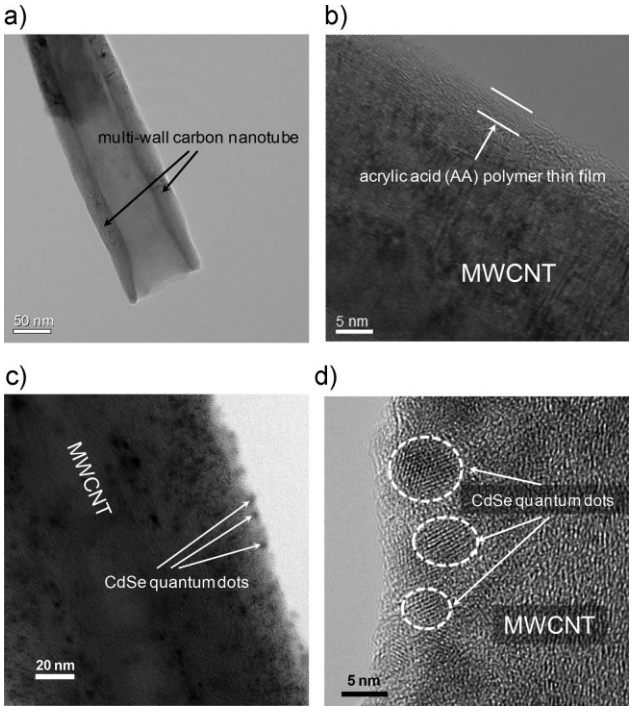

Figure 7. a) TEM image of an uncoated, original MWCNT, b) HRTEM image showing plasma deposited AA polymer thin film (~3 nm) on CNT, c) TEM image of the crystalline CdSe QDs (CNT–QD_{600}) deposited on the surface of CNT, and d) HRTEM imaging showing the lattice structures of both QD_{600} and CNT.

shows bright-field TEM image of an original MWCNT. As can be seen in this figure, the CNT has an open end with an outer diameter of 80 nm and inner diameter of 50 nm, respectively. Figure 7b shows an HRTEM image of the surface-functionalized CNTs. An ultrathin AA film of 3 nm is clearly evident on the outer surface of the nanotube after plasma polymerization (Fig. 7b). The characteristic lattice fringe spacing for carbon can be seen in contrast to the amorphous AA film. The AA film appears to be quite uniform, covering the outer surface of the nanotube.

As can be seen in Figure 7c, the QDs exhibit a dark contrast with an average particle size of 5–10 nm, randomly distributed on the surface of the nanotubes. In the bright-field TEM image of Figure 7c, these QDs appear to be light gray on the CNT surface with some aggregated clusters. Figure 7d shows an HRTEM image of surface conjugated QDs. As can be seen in Figure 7d, the QDs are quite evenly distributed and embedded on the surface of the CNT. The lattice image of QD indicates the crystalline features of CdSe/ZnS QDs deposited on the surfaces of the CNTs. Very similar TEM images have been obtained from QD_{800} (QD with emission of 800 nm) conjugated on CNTs. One of these HRTEM images is shown in Figure 8. As can be seen in this figure, the interlayers of the CNT and lattice of QD_{800} are well resolved in the HRTEM image.

Figure 9 compares the fluorescent spectra of uncoupled QD_{800} and the CNT–QD_{800} coupling product. As is seen in this figure, the maximum emission of the uncoupled QD (dash dot line) is at 795.6 nm, which is consistent with the specification of the commercial product. For CNT-conjugated QD_{800}, the maximum

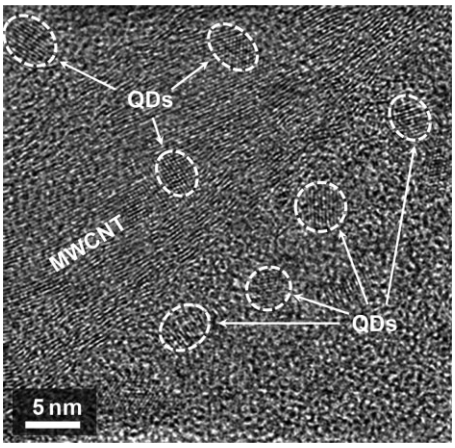

Figure 8. HRTEM image of the crystalline CdSeTe/ZnS QD (QD_{800}) deposited on the surface of the CNT (CNT–QD_{800}).

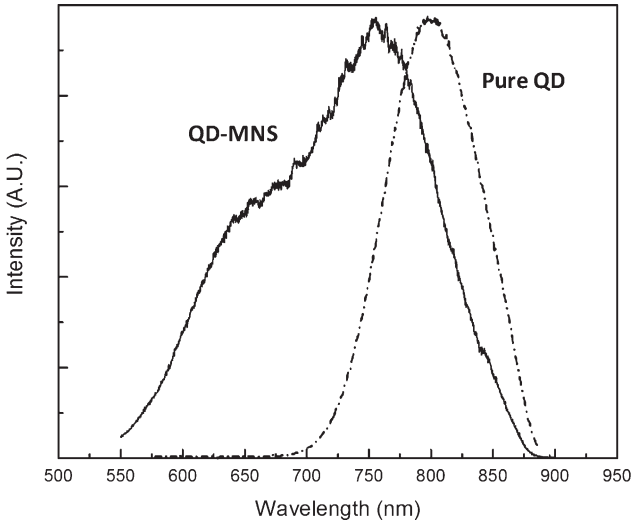

Figure 9. The fluorescent emission spectra of the pure QD and CNT–QD_{800}. The maximum peak at 795.6 nm is the typical emission of QD_{800}. The blueshift from CNT–QD and a broad shoulder around 650 nm may be associated with the interactions and the background emissions of the CNTs. Reproduced with permission from Reference [130], copyright 2008 Wiley-VCH.

emission (solid line) is shifted to 752.5 nm, with a broad shoulder around 650 nm.

2.4. Conjugation of Quantum Dots on Fe_3O_4/Polystyrene (PS) Composite Nanospheres

Among many possible nanosubstrates, a more fascinating novel nanocomposite has been recently developed, namely Fe_3O_4–PS MNSs. As has been well established, for some medical applications such as hyperthermia, the nanoparticles have to be superparamagnetic as they disperse in the fluid under zero-magnetic field. However, micrometer-sized Fe_3O_4 often exhibits

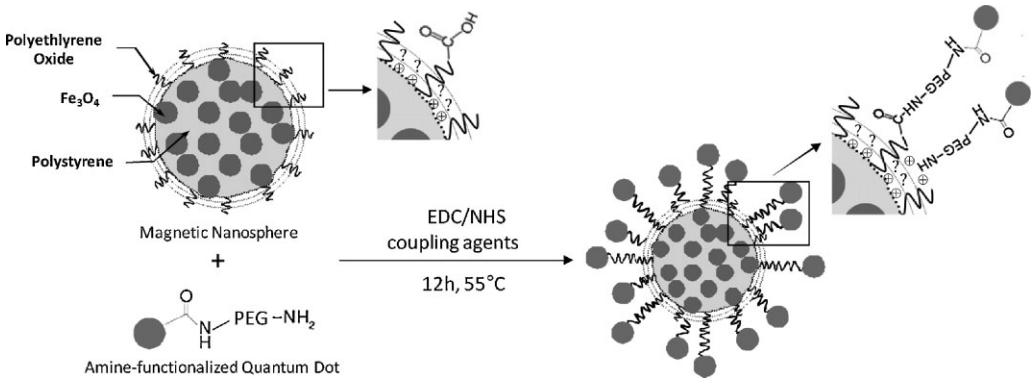

Figure 10. Schematic diagram illustrating surface-immobilized QDs on magnetic PS nanospheres. Reproduced with permission from Reference [128], copyright 2009 Wiley-VCH.

ferromagnetic behaviors with irreversible hysteresis curves. The superparamagnetic property can be effectively obtained by synthesizing monodispersed, nanometer-size Fe_3O_4 particles.[104–106] Although Fe_3O_4 can be rendered superparamagnetic by reducing the size to the nanometer-range, magnetic moments are also significantly reduced. In order to keep the nanoparticles superparamagnetic while retaining high magnetic moments for a variety of applications, the so-called MNSs have been synthesized by a mini-emulsion/emulsion polymerization method.[107]

The novel concept is based on a unique nanostructure of PS nanospheres fabricated within a narrow size distribution (~100 nm) that contain Fe_3O_4 nanoparticles (5–10 nm) embedded in their matrices. In this way, superparamagnetism is not only ensured by the nanometer-size Fe_3O_4, but is also caused by high concentration in a spherical PS matrix for exhibiting high magnetic moments. As discussed before, for simultaneous in vivo imaging and treatment, two major physical properties are needed in the nanocarrier: i) superparamagnetism for hyperthermia and ii) fluorescence for in vivo imaging. Other requirements include monodispersity, surface functionalization with conjugation of biological molecules, and anti-cancer drug-storage capability. Our research has been centered on these requirements in the development of integrated multifunctional nanosystems.

Based on above considerations, the first step is to conjugate QDs on MNSs. A schematic representation of the nanostructure design used to produce MNSs with surface-immobilized QDs (QD–MNS) is shown in Figure 10. Conjugated QDs on the surface of MNSs provides the fluorescent property needed for in vivo imaging. The spherical shape and monodispersity of the QDs allow control of surface functionalization with suitable ligands that facilitate effective tumor-cell targeting. A high fraction of Fe_3O_4 nanoparticles inside the PS matrix will exhibit much stronger magnetic moments for hyperthermia treatment of cancer. The MNS dimension is controlled in the range of 100 nm; a size medically preferred for clinical applications.[108]

To synthesize the nanocomposite depicted in Figure 10, CdSeTe/ZnS QDs have been dispersed and conjugated onto MNS, by using a combined strategy of covalent coupling and electrostatic adsorption. The carboxyl groups resulting from auto-oxidation and partial cleavage of ethylene oxide subunits of MNS-incorporated polysorbate[109] allow covalent coupling of the amine-functionalized QD using conventional carbodiimide chemistry.[110]

Figure 11a shows the HRTEM image of QD–MNS particles. The spherical shape of the PS–Fe_3O_4 composite particles can be clearly seen in this figure. Within the PS nanosphere, the Fe_3O_4 nanoparticles (dark) are embedded in the PS (light) matrix at a

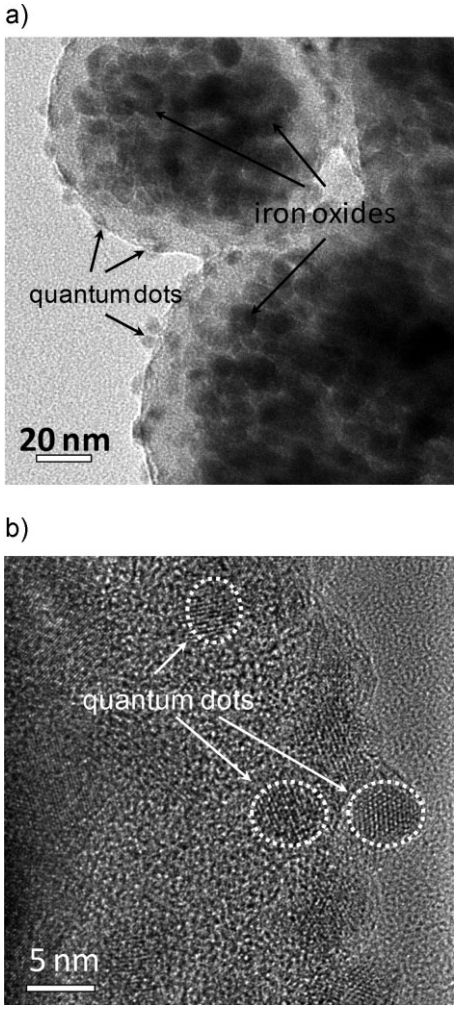

Figure 11. a) Bright-field TEM image of surface-conjugated QDs on MNS; b) HRTEM image depicting surface lattice structures of fabricated MNS–QD_{800}.

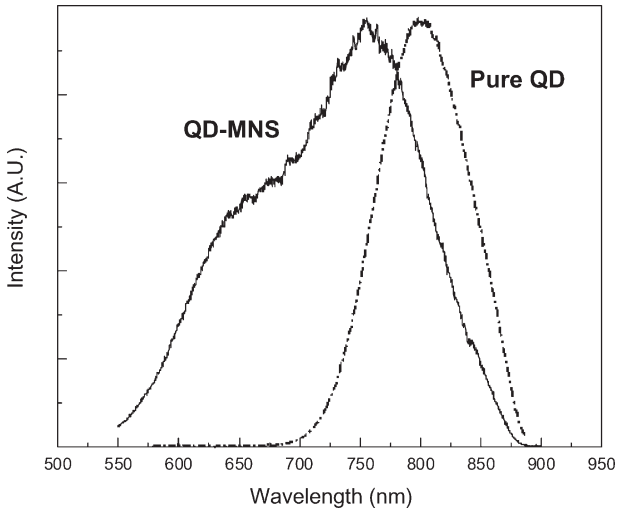

Figure 12. The emission spectra of pure QD_{800} and the MNS–QD_{800}. Data from Reference [128].

high concentration. ODs can also be seen on the surface of the nanospheres in Figure 11a. An HRTEM image of QD–MNS (Fig. 11b) further supports random distribution of surface-associated QDs on the composite nanospheres. A Fourier-transformed image of a randomly selected nanoparticle on the nanosphere surfaces can be indexed as ZnS. These data provide experimental evidence of successful immobilization of the commercial QDs onto the surface of composite PS nanospheres.

Fluorescence of CdSeTe/ZnS QD has been observed at room temperature from the MNS–QD sample (Fig. 12). As shown in this figure, the peak is broad with a maximum around 770 nm. A blueshift can be seen in this figure in comparison with the emission of isolated QDs. For the commercial QDs used in this experiment, the maximum fluorescence is at 800 nm.

2.5. Polymer Micelles for Imaging and Drug Delivery

All nanosystems introduced above are mainly based on inorganic materials. As is well known, there have been extensive research activities in developing polymer-based nanomaterials for imaging and drug delivery. Peng et al. (c.f. Refs. [117–119]) have pioneered a new approach in synthesizing temperature- and pH-sensitive polymer micelles with multiple functions that can be used for medical imaging and diagnosis.

Polymer micelles are defined as self-assembled core–shell nanostructures, typically with hydrophobic core and hydrophilic shell, formed in aqueous solutions from copolymers. In recent decades, polymer micelles have been extensively explored as drug-delivery vehicles due to their unique advantages.[111] Firstly, hydrophobic drugs can be readily entrapped in micelle cores and transported at much higher concentrations compared to naked ones.[112] Secondly, hydrophilic polymer chains in the shell form hydrogen bonds with aqueous surroundings to produce a tight shell around the core. Therefore, hydrophobic cores are effectively protected against hydrolysis and enzymatic degradation. In addition, micelles are protected from uptake by the reticuloendothelial system (RES) with prolonged blood half-lives. Thirdly, chemical compositions and molecular weights of blocks can be easily adjusted to control sizes and morphologies of micelles.[113] Finally, as delivery vehicles, polymer micelles can be readily incorporated with multifunctional properties important for tumor treatments.

In most cases, polymeric micelles are synthesized by assembling block copolymers in selective solvents (Fig. 13a).[114,115] Unfortunately, this synthesis can only be performed in very dilute solutions (typically 1 mg mL^{-1}) with low efficiencies and high cost, which largely limits their applications in both scientific studies and practical uses for drug delivery. New synthetic methods have been then developed aiming at high concentrations. For instance, Peng and co-workers have recently reported three high-efficiency routes to produce micelles with concentrations up to 200 mg mL^{-1}, that

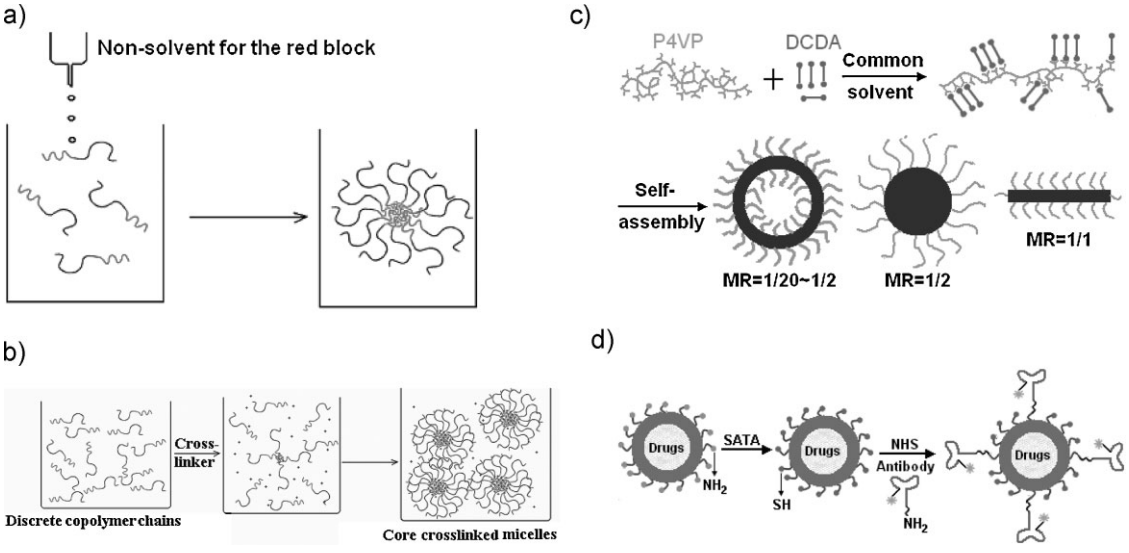

Figure 13. a) Fabrication of polymer micelles by assembling block copolymers in selective solvents; b) schematic illustration of cross-linking induced micellization to prepare polymer micelles with high concentrations up to 200 mg mL^{-1}; c) polymer micelles with tunable morphologies of hollow sphere, solid sphere, and rod synthesized from self-assembly of polymer complexes in common solvents; d) targeting modification of polymer micelle with antibody on its outer surface.

is, crosslinking induced micellization, one-pot approach, and self-assembly of complexes in common solvents.[116–120] In case of cross-linking induced micellization (Fig. 13b),[116] block copolymers were first dissolved in common solvents; crosslinker was then added to crosslink one block; the crosslinked block aggregated to induce micellization. For above methods, polymer micelles with tunable morphologies have been also synthesized (Fig. 13c).[117–119] Micelles with different morphologies may provide drastically different pharmacokinetic properties, as in the case of filamentous nanocarriers which can provide different flow behavior over spherical particles due to anisotropic alignment.

Combination of targeted delivery and controlled drug release is desirable to treat various oncologic diseases. In other words, drugs are expectedly delivered only to cancer cells over an extended period of time without killing the surrounding noncancerous tissue, and then released in a required speed. One efficient approach for targeted delivery is to connect ligands which recognize tumor-specific or tumor-associated antigens on the outer surface of delivery vehicles. A wide variety of targeting ligands, including humanized antibodies, minibodies, and peptides, have been investigated for potential applications in cancer therapy.[120] For instance, the Peng laboratory has reported the accurate targeting of polymer micelles modified with anti-carcinoembryonic antigen (CEA) antibody (Fig. 13d).[121] To determine functional effectiveness of labeled micelles in seeking a labeled target, both of the silica beads without CEA and with anti-CEA antibody modification, as a control, were first located at the inner wall of the microchannel. After passing of the antibody-modified nanoparticles through the microchannel, no drug signals could be detected in the above silica beads by fluorescent spectrometer. As a comparison, the same experiment utilizing the CEA-modified silica beads did produce a strong drug signal. That is, the bioconjugate nanoparticles were only attached to the silica beads with CEA. For controlled drug release, polymer micelles are made of environment-responsive polymers which show a sharp change in properties upon a small or modest change in environmental condition, for example, temperature, light, salt concentration, pH, or combination of several responses.[122–124] For instance, temperature-sensitive polymer micelles made of poly(NIPAAm-*co*-DMAAm) show a very slow release of drug at 37 °C and exhibit much improved releasing speeds with increase in temperatures.[125] This system can be used for hyperthermia treatment. Polymer micelles with targeted delivery, controlled drug releases, and other desirable properties are often called ''smart'' delivery vehicles.

2.6. Cargo-Ship Nanocomposite

Another recent development in the design and synthesis of multifunctional nanosystems is the so-called ''Nano Cargo-Ship'' that involves specially modified lipids and anti-cancer drugs.[126] To have controlled release of drugs that are protected from the body's natural defenses, Park et al.[126] designed a new structure by modifying lipids that are circulating in the bloodstream for a prolonged time period in order to achieve the most effective therapies. Several nanocomponents–QDs, superparamagnetic iron oxide, and anti-cancer doxorubicin–are placed in the ship's hold as depicted in Figure 14. The iron oxide particles are for MRI imaging before surgery that can locate the tumor. The QD fluorescence will assist the surgeon during the operation for removal of the tumor parts. The release of the drug can treat the tumor in a controlled and localized fashion.

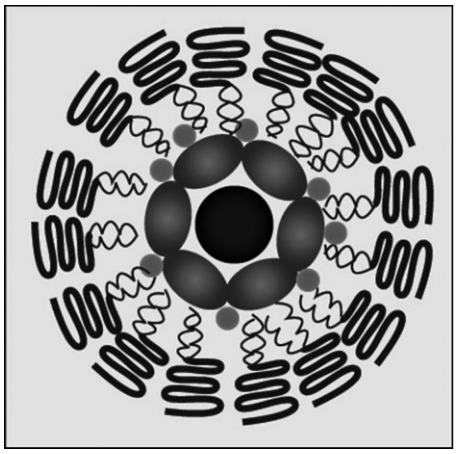

Figure 14. Schematic diagram showing the nano ''Cargo-ship'' [126]. The center sphere represents Fe_3O_4 as an MRI contrast agent; elliptical shaped particles surrounding the center Fe_3O_4 are the anti-cancer doxorubicin; the smaller spheres are QDs for imaging, and outer structures are modifying lipids. Reproduced with permission from Reference [126], copyright 2008 Wiley-VCH.

3. In Vivo Imaging by Multifunctional Nanosystems

Based on the successful integration and developments of multifunctional nanosystems described above, biomedical related experiments including in vivo imaging, drug storage, and targeting have been carried out using QD-conjugated nanocarriers such as HAs, CNTs, and MNSs. It should be noted the concept of QD conjugation on different nanoparticles is intended for achieving simultaneous in vivo diagnosis and treatment. The combination of the magnetic nanoparticles and QDs can also be used in the so-called two-mode imaging, that is, a mechanism switching between MRI and optical imaging for more accurate diagnosis of cancer.[127] Thus, the purpose intended is to construct a nanosystem that possesses biomedically required functionalities: strong fluorescence for in vivo imaging, superparamagnetic for hyperthermia, two-mode MRI/fluorescent imaging, surface functional groups for conjugation of biological molecules needed in cell targeting, hollow structures for drug storage, and biodegradability and biocompatibility.

One of the challenges in deep-tissue imaging is the autofluorescence in the background that severely interferes with the quality and resolution of the images. Although QDs exhibit strong visible emissions, a few experiments have been carried out on QD-conjugated nanosubstrates in deep-tissue in vivo whole-body imaging. As such, we have systematically conjugated QDs on a variety of nanocarriers including hydroxylapatite (HA-QD), CNTs-QD, and Fe_3O_4/PS composite nanospheres (MNS-QD).[128] Initial in vivo imaging experiments have been attempted in mice by

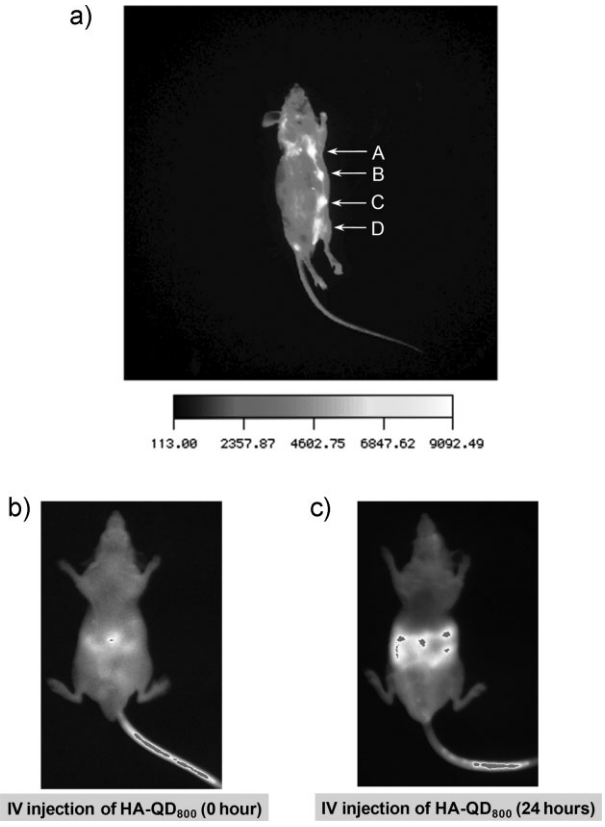

Figure 15. In vivo fluorescence images of a) from HA–QD_{600} intramuscularly injected at positions A, B, C, and D; the fluorescent intensities decrease from 7 900, 6 800, 5 900 to 4 700. The suspensions of HA–QD_{600} are diluted by PBS at different concentrations of HA nanoparticles (A, 10 μmol mL^{-1}; B, 5 μmol mL^{-1}; C, 2.5 μmol mL^{-1}; and D, 1.25 μmol mL^{-1}); b) HA–QD_{800} i.v. injected into the tail vain under 720-nm excitation and c) HA–QD_{800} i.v. post-injection after circulation for 24 h. Reproduced with permission from Reference [89], copyright 2008 the Institute of Physics.

both direct and intravenous injections of the QD conjugated nanocarriers with varied concentrations in the solutions.

3.1. In Vivo Imaging by HA–QD

For HA–QD, we have used QDs with 600-nm (HA–QO_{600}) and 800-nm (HA–QO_{800}) emissions, respectively. The in vivo imaging of the mice has been studied by using the Kodak Whole-Mouse Image Station (Kodak 4000MM). The excitation light from a high-intensity lamp with the 10× zoom lens is directed through the selected excitation filter to the mice. The red excitation of 525 nm is selected as the HA–QD has a high absorbency in this range. The red-light excitation also improves the visualization at increased tissue depth.

The hypodermic injection of HA–QD_{600} into various regions of the mice has been performed. The images were collected after exposure of 2 min (Fig. 15). The suspensions of HA–QD_{600} were diluted by phosphate-buffered saline (PBS) at different HA-nanoparticles concentrations (A, 10 μmol mL^{-1}; B, 5 μmol mL^{-1}; C, 2.5 μmol mL^{-1}; and D, 1.25 μmol mL^{-1}). These suspensions were injected by the volume of 10 μmL into various abdomen locations from head to the tail. As shown in Figure 15a, from the injection positions A, B, C, and D, the fluorescent intensities decrease from 7 900, 6 800, 5 900 to 4 700 (arbitrary units). The position A with the highest dosage of 10 μmol mL^{-1} exhibits the brightest image, while its intensity graduate decreases as the HA–QD concentration is diluted. However, even for the lowest concentration of 1.25 μmol mL^{-1}, as marked at position D, the image still exhibits pronounced fluorescence intensity. The intensity bar indicates the relative fluorescence index of the injection position. Comparing to the mice background fluorescence of 2 300 (arbitrary units), the injection positions of HA–QD_{600} have fluorescent intensities in the range from 4 600 to 9 000. These intensities from the injected body area show significant uptake of the HA–QD_{600} in the underskin tissues of the live animal. It demonstrates that the fluorescence intensities correlate to the concentrations of the HA–QD_{600} administered to the mice. The intensive in vivo images obtained in this study indicate that the HA–QD_{600} can be easily imaged by hypodermic injection.

These results clearly indicate that HA–QD can serve as an ideal biomarker candidate for in vivo imaging. However, it has been found that the emissions in this visible range below 700 nm can easily overlap with those autofluorescence from the animal bodies as a background noise, such as the autofluorescence signals from skin wrinkles in the upper body. To further enhance the imaging contrast particularly for deep tissue imaging, the QD with longer emission wavelength (800 nm) was used to conjugate on the HA nanoparticles (HA–QD_{800}). With the same procedure described above, the mice were i.v. injected with HA–QD_{800}. The fluorescent microscopy images of the HA–QD_{800} solution are shown in Figure 15b and c. Figure 15b shows the imaging result obtained from HA–QD_{800} immediately after i.v. injection into the tail veins of the mice. The enhanced contrast in these images indicates that the HA–QD_{800} can be visualized against an essentially black background, without interference from the mouse autofluorescence. As a result of high quantum yield and high absorbency, the fluorescence of HA–QD_{800} in the superficial vasculature (the whole tail vein in Fig. 15b) is readily visible immediately after injection. However, at this early post-injection time, HA–QD_{800} cannot be imaged in organs; some emission is seen from the stomach, from food autofluorescence. Upon migrating for 24 h, a fluorescent image (Fig. 15c) shows strong signals of HA–QD_{800} in both liver and spleen. The intense contrast of the inner organs with the mouse low-noise background demonstrates the successful i.v. injection and circulation of HA-QD_{800} in vivo. The accumulation of HA-QD_{800} in liver and spleen is due to the nanoparticles being easily uptaken by the RES (most notably in the liver). The efficient circulation and delivery of HA–QD_{800} in the live animal shows the high potential of HA–QD_{800} as a biomarker.

Based on these experimental results, it can be seen that not only can the QDs be well conjugated onto the HA nanoparticles, but also resulted in sharp in vivo imaging. The in vivo results presented here are initial attempts to see the possibilities of in vivo imaging by QD-conjugated nanosubstrates. The current research activities deal with subcutaneous and intravenous injections of HA-QD in a sequence of cancer xenograft mice. With these preliminary data, it is therefore possible to explore in vivo imaging from other QD-conjugated nanosubstrates such as CNTs.

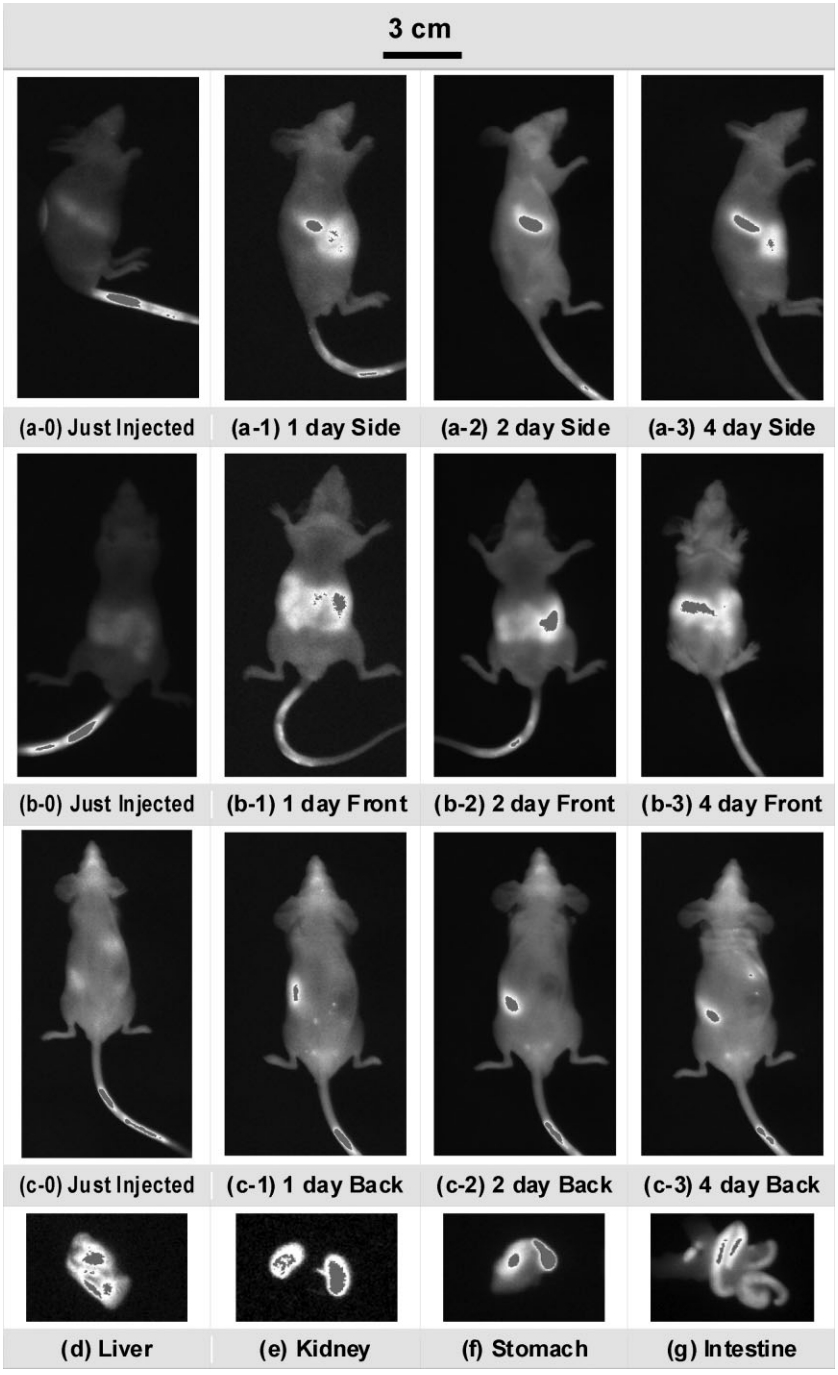

Figure 16. In vivo fluorescence images of CNT-QD i.v. injected into nude mice and imaged after circulation at various time intervals; a-0 to a-4) the images taken from the side of mice; b-0 to b-4) from the front; c-0 to c-4) from the back of mice, and d–g) organ images taken after having sacrificed the mice on the sixth day of post-injection. These pictures show prominent CNT–QD uptaking in the liver, kidney, stomach, and intestine. Reproduced with permission from Reference [130], copyright 2008 Wiley-VCH.

3.2. In Vivo Imaging by QD-Conjugated Carbon Nanotubes

As has been found in the in vivo experiments using HA–QD, one of the key issues involves the intensity and the frequency of the emissions from the QD-conjugated nanoparticles. For deep-tissue imaging, highly intense emissions are required at frequency in the near infrared range (>700 nm). In the in vivo imaging experiments of CNT–QD, it has been found that 800-nm-QD-conjugated CNTs experienced considerable blueshift, as shown in Figure 12. As seen in Figure 12, the maximum emission of the uncoupled QD (dash dot line) is at 795.6 nm, which is the consistent with the specification of this commercial product. For CNT-conjugated QD, the maximum emission (solid line) is shifted to 752.5 nm, with a broad shoulder around 650 nm.

This blueshift has been found to be associated with the surface-charge-induced Stark effect on the quantum-confined emitting state of QDs conjugated on the surface of CNTs.[30] The local electrostatic field on the functionalized CNT surface could influence the excitonic states of QDs by inducing a Stark shift up to 0.59 eV. This is much greater than the electron–hole binding energy. The Stark shift of QD luminescence exhibits a linear and quadratic function of the local field, which is consistent with the previous observations for single free QDs.

Based on extensive previous developments of multifunctional nanosystems, we have carried out a systematic experiment on a CNT-based assembly. The nanostructure design for in vivo imaging and drug storage is schematically illustrated in Figure 2. The hollow core and polymer-coated surfaces of the nanotube can be used to store antitumor agents such as paclitaxel as a consequence of non-covalent adsorption. The CNTs are surface functionalized with an ultra-thin poly(D,L-alctide-*co*-glycolide) (PLGA) coating by plasma polymerization. Quantitative determination of paclitaxel drug loading has been achieved for this novel nano-assembly. For deep tissue imaging, the outer surface of the nanotube is conjugated with QDs.

The experimental procedures for in vivo imaging are explained briefly in the following. CNT-QD_{800} was i.v. injected via tail vein into mice. The in vivo images were taken from live animals at various time intervals (i.e., immediately after injection, 1, 2, and 4 days) using the Kodak 4000MM Whole-Mouse Imaging System (Carestream Health, Inc., Rochester, NY; excitation, 725 nm; emission, 790 nm). Figure 16 shows grayscale imaging results obtained from CNT-QD_{800} i.v. injected into the tail vein of mice (red color indicates the area where fluorescent emission is saturated). The fluorescence of CNT-QD_{800} in the superficial vasculature (tail veins in Fig. 16a-1, b-1, c-1) is readily visible under the Kodak Imaging System immediately after injection. However, no fluorescent images can be observed in organs and tissues at this early post-injection stage. After circulation for 2–4 days, the images (Fig. 16a-2 to a-3, b-2 to

b-3, c-2 to c-3) appear with strong signals of CNT–QD_{800} in several organs of live animal including liver, kidney, stomach, and intestine. These fluorescent images are sharp with high resolutions in an essentially black background. No significant interference by autofluorescence of the animal was observed. The sharp images indicate that QDs at the near-infrared range can provide clear fluorescence visualization in live animals. To confirm CNT–QD_{800} uptake in these organs, the liver, kidney, stomach, and intestine were harvested for ex vivo imaging (Fig. 16d–g). The strong fluorescent emissions in these organs under epi-UV illumination are consistent with the images from Figure 16a–c, as a result of the emission fluorescence from CNT–QD_{800}. These experimental results show that CNTs with surface conjugated QDs can serve as viable nanotools for deep tissue in vivo imaging.

3.3. In Vivo Imaging by QD-Conjugated Fe_3O_4–Polystyrene Nanospheres

In vivo imaging experiments have been carried out in live mice with the QD-conjugated Fe_3O_4–PS nanospheres (QD-MNS).[128] The imaging facility used was the Kodak Imaging Station, with in vivo fluorescence monitored before and after i.v. injection of QD-MNS (10 mg mL^{-1} in PBS, 100 μL of QD-MNS per animal) in nude mice via tail vein.

The grayscale fluorescence images are shown in Figure 17, from both control and QD–MNS-injected animals. It can be seen in Figure 17a that certain ventral regions exhibit autofluorescence in the control mouse. However, significant fluorescence signals appear after one day post-injection, attributable to QD–MNS in the anatomical region of the spleen (Fig. 17b).

To investigate local biodistributions of QD–MNS and associated imaging, animals were sacrificed and organs harvested. The ex vivo fluorescence images of the spleen are shown in insets of Figure 17a and b, respectively, which indicate the accumulation of QD–MNS in this organ of the treated mouse. No significant fluorescence was registered in the ex vivo image of the untreated control animal. For histological evidence, tissue was embedded in optimal cutting temperature compound (EMS, Hatfield, PA). Ten micrometer cryosection was prepared at −20 °C using an UltraPro 5000 cryostat (Vibratome Comp., Louis, MO, USA). Microscopic evaluation of these sections in bright-field (Fig. 17c) and fluorescence (Fig. 17d) mode clearly indicate the accumulation of fluorescent QD-MNS in non-sinusoidal mouse spleen with limited distribution into red pulp reticular meshwork. These data are direct evidences that in vivo administration of QD–MNS results in detectable fluorescence signals in a live animal. Current research deals with surface functionalization with antibodies for cell targeting and drug storage for localized treatment.

Magnetic and hyperthermal properties of polyethylene oxide-modified PS–MNS have been evaluated previously.[22–29] In this study, magnetic hysteresis measurements and hyperthermia experiments were performed on QD-functionalized MNS. The heating rate of MNS is measured using Hilger's technique.[27,129] For comparison, two samples were measured under the same experimental conditions. The detailed experimental procedures can be found in Refs. [22,27,129]. The frequency and amplitude of the magnetic field used were 63 kHz and 7 kA m^{-1}, respectively. A total of 0.1 mL magnetic fluid that contained 50 mg MNSs with an average diameter of 100 nm dispersed in iodinated oil was placed in a sample container. An optical fiber thermometer probe (FTI-10; FISO Co., Ltd., Canada) was used inside the container for monitoring the temperature change. The temperatures of both samples increase almost linearly up to 31 °C for a heating time of 20 min. Continued heating results in steady temperature increase up to 45 °C, as previously demonstrated for the Fe_3O_4 nanoparticles.[128,129] The heating mechanism has been attributed to the Néel relaxation behavior, a well established model in hyperthermia.[22,24–29]

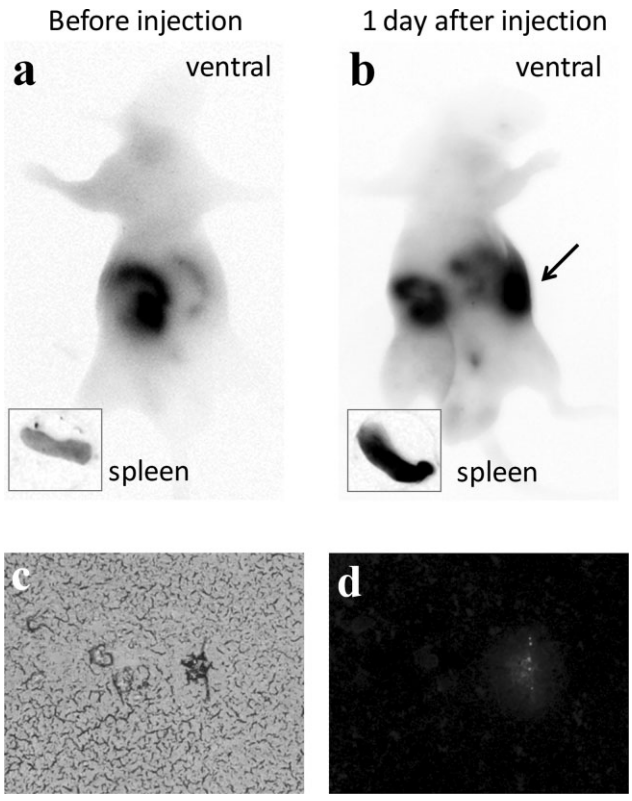

Figure 17. In vivo and ex vivo images after intravenous injection of QD–MNSs in nude mice. Red fluorescence signals indicate QD-MNS accumulation in the spleen; a) in vivo fluorescence before injection; b) in vivo fluorescence one day after injection; c) bright-field microscope image of a histological spleen section; d) corresponding fluorescence image of the same section of tissue shown in (c).

4. Cell Targeting and Drug Storage

Based on a novel nanostructure design, QDs have been conjugated onto the surfaces of the CNT and MNS for in vivo imaging. Anticancer drug has also been efficiently loaded in PLGA-coated CNT. The PLGA-coated CNTs show high loading efficiency for paclitaxel, which demonstrates in vitro antitumor efficacy against human prostate cancer cells.[130,131] ICP-MS studies indicate predominant CNT-QD uptake in liver, kidney, stomach, and intestine following i.v. administration in mice. The development of CNT-QD as a non-invasive optical in vivo imaging and drug delivery system may have a great impact in early detection, diagnosis, and treatment of cancer.

4.1. Cell Targeting

The above experimental results have indicated that deep tissue imaging can be well established by QD-conjugated nanosubstrates that are integrated with multifunctionalities. So far, imaging experiments from live mice have been successful using a variety of nanosystems including HA nanoparticles, CNTs, and Fe_3O_4–PS MNSs. But it must be emphasized that during the imaging tests with these nanosystems they are not surface functionalized with tumor specific ligands or organ targeting moieties. Therefore, the observed biodistribution pattern following i.v. administration reflects the results of non-specific binding and elimination processes. It is expected, however, that coupling with specific targeting ligands such as peptides and antibodies will alter the biodistribution pattern.

Therefore, cell targeting with surface functionalized tumor specific antibodies will be essential in achieving early cancer diagnosis and treatment by these multifunctional nanosystems. One of the experimental approaches for prostate cancer cell-targeting using MNS is schematically illustrated in Figure 18. As shown in this figure, the MNS can be conjugated to the monoclonal mouse anti-human prostate specific membrane antigen and Alexa Fluor 594 goat anti-mouse IgG. The secondary antibody can be conjugated to the carboxyl groups on the MNS surface using carbodiimide coupling chemistry. The primary antibodies are then attached on the secondary antibody by recognizing them. Some preliminary immunocytochemical data have indicated strong and specific binding of the anti-PSMA conjugated MNS to a human prostate cancer cell line, LNCaP, which is known to express PSMA on the cell surface.

Immunocytochemical studies of anti-PSMA-conjugated MNSs binding activity in LNCaP prostate cancer cells has been carried out using goat anti-mouse IgG, Alexa Fluor 594. LNCaP cells were stained successfully in the presence of the anti-PSMA bioconjugated on the MNSs surface and minor staining was detected in LNCaP cells exposed to the secondary antibody-conjugated MNSs in the absence of anti-PSMA. This establishes that anti-PSMA conjugated MNS can be used as a cell surface-specific marker for LNCaP prostate cancer cell lines. In a similar way, CNTs and other nanosubstrates can also be conjugated with cancer antibodies for cell targeting.

4.2. Drug Storage and Cytotoxicity

Another challenge in cancer diagnosis is localized delivery of drugs in a controlled fashion. While accomplishing in vivo imaging and cell targeting, for effective cancer treatment, anti-cancer drugs need to be stored within the nanosystem for local delivery to the lesions. Since these nanosubstrates exhibit quite different structural characteristics, the drug loading methods may differ. We have carried out drug loading experiments for both CNTs[130] and MNSs.[128]

Paclitaxel is an antitumor agent demonstrating significant activity in clinical trials against a variety of solid tumors.[132–134] However, due to its high hydrophobicity and low therapeutic index, its application has been limited. Therefore, a wide variety of nanomaterials for paclitaxel delivery system such as liposomes, nanoparticles, macrospheres, and soluble polymers have been investigated. Among these new drug delivery systems, polymeric materials have drawn attention as promising carriers for anti-cancer agents because of their higher stability and the possibility to surface functionalization. In particular, PLGA is a biodegradable polymer and used most often for drug delivery.

In our previous research, CNTs incorporated with PLGA were developed for paclitaxel delivery by plasma polymerization and emulsion technique. The drug-loading efficiency of PLGA-coated CNTs and their cytotoxicity on human prostate cells have been investigated.[130] Based on the previous experimental results in Ref. [130], further investigation on drug storage and cytotoxicity has been carried out.

In this current research, paclitaxel-loaded CNTs were prepared by the emulsion technique.[130,35] Briefly, 2.5 mg PLGA-coated CNTs and 2.5, 1.25, and 0.625 mg of paclitaxel were dissolved in DCM under ultrasonication for 15 min. For the control, an identical experiment was carried out without any paclitaxel. The organic solution was added into water and the oil-in-water emulsion was formed by sonicating with energy output of 5 W in a pulse mode. The oil-in-water emulsion was sonicated under reduced pressure for evaporating the organic solvent, DCM and then, the sample was centrifuged and washed three times. Finally, the gathered sample suspended in water was freeze-dried overnight and kept refrigerated.

High-performance liquid chromatography (HPLC) was used for determining the efficiency of drug loading on PLGA-loaded CNTs.

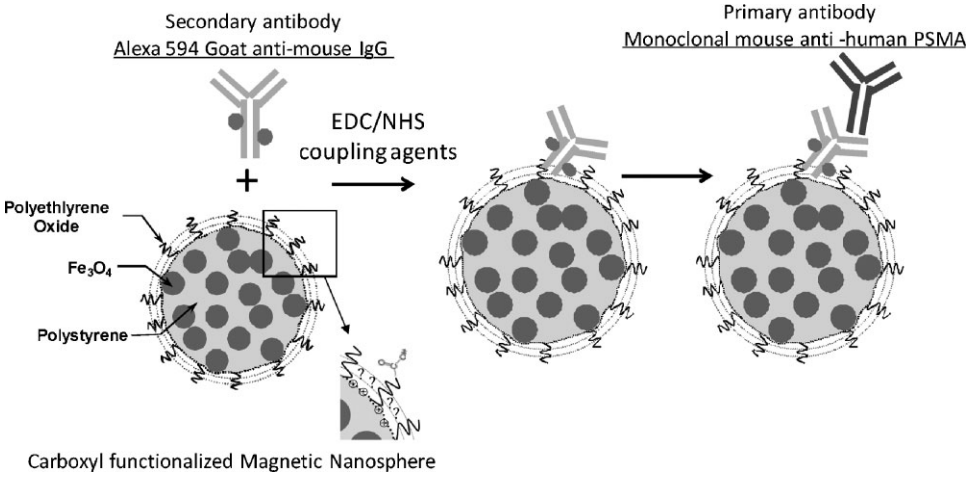

Figure 18. Schematic diagram showing the conjugations of antibodies to MNSs. The MNS is covalently conjugated to the secondary antibody, Alexa 594 goat anti-mouse IgG in the presence of EDC. The primary antibody is bonded to the secondary antibody by high affinity.

The mixture of 50/50 v/v acetonitrile and water was used as a mobile phase. Briefly, CNTs loaded with a known amount of paclitaxel were dissolved in 500-μL acetonitrile and kept in an incubator at 37 °C for 0–6 h to release all paclitaxel from the CNTs. The samples were then centrifuged to remove CNTs. To draw standard plot of paclitaxel in both DMSO and acetonitrile, various concentrations between 0.25 and 0 mg mL^{-1} were tested by HPLC. The drug-loading efficiency is expressed as the ratio of real amount of drug loaded on the CNTs to initial amount of drug for the drug-loaded CNTs.

The cytotoxicity of paclitaxel-loaded CNTs was evaluated by MTT assay using the PC3 mm^2 human prostate carcinoma cells. Cells were cultured in EMEM supplemented with 5% FBS, nonessential amino acids, sodium pyruvate, vitamin A, and glutamine at 37 °C in a balanced air humidified incubator with an atmosphere of 5% CO_2. Cells in exponential growth phase were harvested by a 2-min treatment with a 0.25% trypsin/0.02% EDTA solution and maintained by periodic dilutions with fresh medium. Effects of paclitaxel-loaded CNTs on cell growth in vitro were evaluated by MTT assay. Cells in 100-μL EMEM-1% FBS were plated at a density of 1 000 cells in a 96-well plate. After an overnight incubation culture period, the cells were incubated in EMEM/1% FBS containing different concentrations of paclitaxel or paclitaxel-loaded CNTs at 37 °C in 5% CO_2 for 4 days. During this period, the cells grew exponentially without change of medium. After 4 days, 3-(4,5-dimethylthiazol-2-yl)-2,5-diphenyltetrazolium bromide (2 mg mL^{-1} in PBS) was added to the cultures at 0.05 mL per well during the final 2 h of incubation. The medium was then carefully removed, and the dark blue formazan was dissolved in 100 μL per well of DMSO. The absorbance of each well was measured with a FluoStar Optima multi-detection microplate reader (BMG Labtechnologies, Durham, NC, USA) at 570 nm. The percentages of growth inhibition were calculated according to the following formula: growth inhibition (%) = (1 − Abs_{570} of treated group/Abs_{570} of control group) × 100.

A standard curve of paclitaxel in acetonitrile solution is shown in Figure 19 to calibrate paclitaxel concentration. The curve is linear with the range of 0.25–0 mg mL^{-1} with a correlation coefficient of $R^2 = 0.998$ and the acetonitrile solution does not interfere with paclitaxel peak. Table 1 shows the paclitaxel-loading efficiencies of

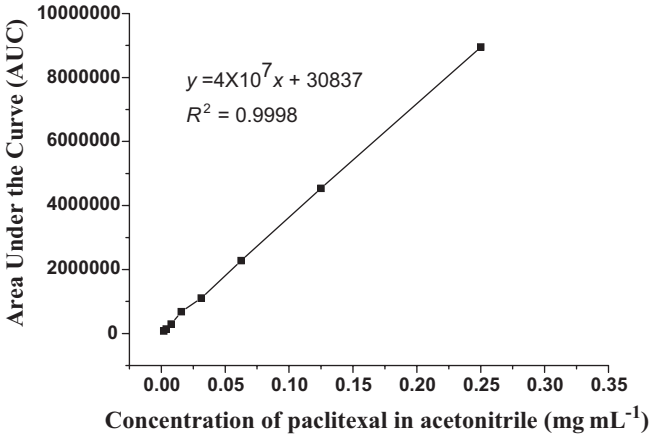

Figure 19. Standard curve of paclitexal in acetonitrile in the range of 0–0.25 mg mL^{-1} concentration.

Table 1. Paclitaxel-loaded efficiency of PLGA-coated CNTs from HPLC [a].

Incubating time [h]	AUC	Conc. [mg mL^{-1}]	[%] of loading
0	6889226	0.1918	76.74
1	6870555	0.1913	76.53
2	6904272	0.1923	76.90
4	6834890	0.1903	76.13
6	6845667	0.1906	76.25
Mean	**6868922**	**0.1913**	**76.51**

[a] The theoretical concentration of paclitaxel loaded in CNTs is 0.25 mg mL^{-1}, supposing that all the paclitaxel is loaded on the CNTs.

PLGA-coated CNTs with various incubation times. The 34% weight ratio of paclitaxel to PLAG-coated CNTs was used in this research (i.e., 8.5 mg of paclitaxel and 25 mg of CNTs.). A certain amount of paclitaxel-loaded CNTs was diluted in a solution to 0.25 mg mL^{-1}. This means that a given amount of paclitaxel-loaded CNTs has loaded 0.25 mg of paclitaxel, assuming that all initial paclitaxel was loaded on CNTs. To determine drug loading, the known amount of paclitaxel-loaded CNTs was suspended in acetonitrile at 37 °C for 0–6 h., and paclitaxel was released from the CNTs.

From Table 1, it can be seen that paclitaxel is released immediately after being in acetonitrile. PLGA-coated CNTs can achieve around 76% drug loading efficiency. Although there is possibility that the PLGA coating layer could be dissolved in a solvent, and may form its own micro- or nanoparticles during emulsion process, the PLGA-coated CNTs have a high loading efficiency in comparison with polymer nanoparticles by emulsion method, especially in high drug/materials ratio.[135,136]

The cytotoxicity of paclitaxel-loaded CNTs on growth of cells in vitro was evaluated by MTT assay. As can be seen in Figure 20, over 60 nM of concentration, both paclitaxel and paclitaxel-loaded CNTs inhibit growth of cells by 85%. However, below 60 nM of

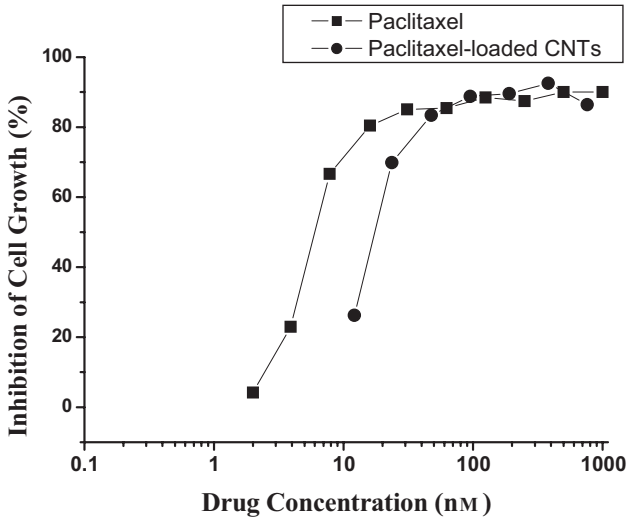

Figure 20. Effects of paclitaxel and paclitaxel-loaded CNTs on PC3MM2 cells. The cells are treated with various concentrations in medium supplemented with 3% FBS for 4 days.

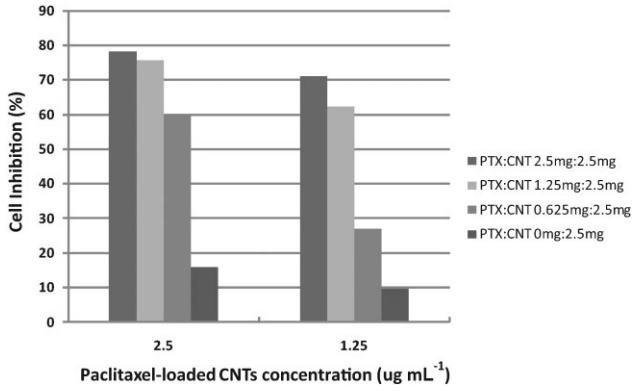

Figure 21. Effects of varying paclitaxel:CNT ratios (2.5 mg:2.5 mg; 1.25 mg:2.5 mg; 0.625 mg:2.5 mg; and 0 mg:2.5 mg) on the cytotoxicity of PC3 mm^2 cells by growth inhibitions of human PC 3 mm^2 prostate cancer cells. Tumor cells are treated with CNTs or paclitaxel-loaded CNTs dispersed in culture media supplemented with 1% FBS for 4 days.

concentration, paclitaxel shows a much higher inhibition of cell growth compared to drug-loaded CNTs. The cytotoxic effect of paclitaxel at 16 nM of concentration demonstrates 80% inhibition in cell growth, as compared to 26% inhibition at the same concentration of paclitaxel from paclitaxel-loaded CNTs. This is due to drug release being affected by the PLGA coating layer on CNTs. It was reported that the in vitro drug release from the paclitaxel-loaded PLGA nanoparticles exhibit less than 30% of encapsulated drug after 10 days.[137] In this study, a faster drug release was achieved as a result of PLGA coating on CNTs.

Figure 21 shows the effects of paclitaxel to CNTs ratio (2.5 mg: 2.5 mg; 1.25 mg:2.5 mg; 0.625 mg:2.5 mg, and 0 mg:2.5 mg) on the cytotoxicity for PC3 mm^2 cells. There is a consistent correlation between the ratio of paclitaxel to CNTs and the cell growth inhibition. It is clear that a higher concentration of paclitaxel in a solvent results in more paclitaxel to be loaded on the CNTs. However, it is shown that the effect of CNT without paclitaxel on the cell growth is less than 10% of inhibition at the concentration of 1.25 $\mu g\ mL^{-1}$.

4.3. Toxicity of Carbon Nanotubes

As is well known, the presence of nanoparticles in the environment has caused considerable concerns.[138] Although there have been extensive experiments carried out to study the toxicity of CNTs, the results have shown different observations. Lam et al. reported the toxicity of single-walled CNTs (SWCNTs) by exposing groups of mice to as-grown SWCNTs containing the metal catalysts.[94] They have found that, when the lungs of mice were treated with SWCNTs, it induced dose-dependent epithelioid granulomas, while no abnormal effects were observed when expositing to carbon black. In vitro cytotoxicity screens on cultured human dermal fibroblasts (HDF) were performed on a set of functionalized SWCNTs by Sayes et al.[139] Their results have shown that, as the degree of surface functionalization increases, the SWNT sample becomes less cytotoxic. Further, surface functionalized SWCNT samples are substantially less cytotoxic than surfactant stabilized SWCNTs. A more recent study by Schipper et al. indicates no evidence of toxicity after having injected functionalized SWCNTs in the bloodstream of mice.[140] Their experimental data on necropsy and tissue histology only show age-related changes. They found that the functionalized SWCNTs persisted within liver and spleen macrophages in a prolonged period of 4 months, but showing no apparent toxicity. Thus, it appears that the toxicity of CNTs may depend on a variety of factors including types of materials, processing methods, surface properties, particle sizes, and even batch conditions.

5. Intelligent Nanosystems for Biomedical Studies: A Future Trend

In fundamental biomedical studies, the development of multifunctional nanosystems also presents significant advantages for sensing, actuating, regulating, and signaling the biological responses in order to have precision controls at cell levels. A typical example is DNA manipulation[141] by nanotechnology, which has been an intensive research due to its key role in gene detection,[142] transfection,[143–145] and therapy.[146] The critical issues in these areas deal with basic understandings of nano–bio interfaces and underlying conditions that dictate the biological feedbacks due to the implant of nanoengineered devices.

In previous studies, a variety of nanomaterials have been developed for biomedical applications, including colloid gold,[147] silica nanoparticles,[148] QDs,[82–87] magnetic nanoparticles,[22–26] and functional polymers.[111–113] However, in most of these developments, the nanomaterials developed are utilized only with their limited and isolated intrinsic properties, be it magnetic, fluorescent, or hyperthermic. Nonetheless, the complicity of a biological system requires intelligent performance of a nanoscale device that can function in a selective, controlled, localized, and predictable manner.

Design and development of multifunctional intelligent nanosystems will pave a new path in the biological manipulation and medical diagnosis. The multifunctionality is based on the structural integration of several nanospecies with unique properties including QDs for in vivo imaging, magnetic nanocomposites for hyperthermia and separation, nanotube capsules for drug storage, and surface functional groups for biological selectivity. Furthermore, biodegradable polymer micelles exhibit pH and temperature sensitive behaviors that are highly desirable in biomedical applications. These combined components provide the needed functionalities in both biological manipulation and medical diagnosis. The intelligent nanosystems utilize integrated functionalities and perform controlled actions such as switching on/off the drug release, signaling to the sensing device, recognizing a specific cell, and monitoring the concentration level in a biological and living system. The development of these multifunctional systems requires both engineering design of the nanostructure and biomedical tuning of the intelligent responses, therefore demanding a true interdisciplinary research in synthesis, nanostructure architecture, surface engineering, and biomedical system integration.

Future research needs to be devoted to the development of intelligent and integrated multifunctional nanosystems that can perform in vivo, real time biomedical imaging, actuating, and

regulating at the subcellular level. The integrated multifunctional nanosystem is designed and equipped with intelligent capabilities that enable the registration of progressive response of the living host, and at the same time, the alteration of active conditions for control, manipulation, and selection. Based on such an intelligent system, not only can superior understanding be established for cell mechanics and tissue interfaces in living system, but also well-manipulated and programmed biological system via artificially engineered intelligent devices.

Acknowledgements

The author is especially indebted to Dr. Zhongyun Dong of the College of Medicine and Giovanni Pauletti of the College of Pharmacy at University of Cincinnati for their invaluable contributions in this work, without which this research would not have been possible. Not only have they provided research visions in critical medical issues, but also very much needed training in biomedical areas for all graduate students who participated in these experiments. Their expertise and experiences in prostate cancer (Dong) and drug kinetics (Pauletti) research, as well as all their state-of-the-art facilities are the foundations of this work. Most of the experimental works in nanoparticle synthesis and characterization; surface functionalization and conjugation, cell targeting, and drug storage were carried out by graduate students: Hoon Sung Cho, Christopher Huth, Yan Guo, Wei Wang, and Feng Wang. The author greatly appreciates their dedications, diligent works, and talents in nanomedicine research. We are also grateful to Dr. Jie Lian of RPI, Dr. Rod Ewing and Lumin Wang of University of Michigan for their excellent and extensive TEM works that form the core microscopy experimental data in this research. Dr. G. K. Liu's laser fluorescent spectroscopy from Argonne National Laboratory provided important optical characterization of all nanoparticles used in this study. Drs. Hongchen Gu and Hong Xu from Shanghai Jiao Tong University supplied us with the most valuable Fe_3O_4 composite nanospheres that were critically needed in the hyperthermia experiments. The author owes intellectual debts to Dr. H. S. Peng of Fudan University and Dr. M. J. Sailor of University of California at San Diego for providing the schematic diagrams on polymer based multifunctional nanomaterials for medical applications (Figs. 13 and 14, respectively). These are valuable and timely contributions to this paper. The support from the National Science Foundation DGE-0333377 and the Institute for Nanoscience and Technology at University of Cincinnati is appreciated.

Received: August 15, 2009
Published online: October 9, 2009

[1] H. Lee, T.-J. Yoon, J.-L. Figueiredo, F. K. Swirski, R. Weissleder, *Proc. Natl. Acad. Sci.* **2009**, *106*, 12459.
[2] A. Villers, L. Lemaitre, J. Haffner, P. Puech, *Curr. Opin. Urol.* **2009**, *19*, 274.
[3] H. Degani, V. Gusis, D. Weinstein, S. Fields, S. Strano, *Nat. Med.* **1997**, *3*, 780.
[4] S. E. Harms, D. P. Flamig, *JMRI-J. Magn. Reson. Imaging* **1993**, *3*, 277.
[5] S. H. Heywang-KoBrunner, R. W. Katzberg, *Invest. Radiol.* **1994**, *29*, 94.
[6] W. A. Kaiser, E. Zeitler, *Radiology* **1989**, *170*, 681.
[7] E. Furman-Haran, R. Margalit, A. F. Maretzek, H. Degani, *J. Magn. Reson. Imaging* **1996**, *6*, 195.
[8] E. Furman-Haran, R. Margalit, D. Grobgeld, H. Degani, *Proc. Natl. Acad. Sci. U. S. A.* **1996**, *93*, 6247.
[9] C. M. Carpenter, B. W. Pogue, S. Jiang, H. Dehghani, X. Wang, K. D. Paulsen, W. A. Wells, J. Forero, C. Kogel, J. B. Weaver, S. P. Poplack, P. A. Kaufman, *Opt. Lett.* **2007**, *32*, 933.
[10] G. C. Alex, J. Huabei, N. H. Steven, D. Matthew, G. C. William, R. G. Stephen, *Cancer* **2006**, *107*, 459.
[11] R. Weissleder, K. Kelly, E. Y. Sun, T. Shtatland, L. Josephson, *Nat. Biotechnol.* **2005**, *23*, 1418.
[12] O. C. Farokhzad, S. Jon, A. Khademhosseini, T.-N. T. Tran, D. A. LaVan, R. Langer, *Cancer Res.* **2004**, *64*, 7668.
[13] J. F. Kukowska-Latallo, K. A. Candido, Z. Cao, S. S. Nigavekar, I. J. Majoros, T. P. Thomas, L. P. Balogh, M. K. Khan, J. R. Baker, Jr, *Cancer Res.* **2005**, *65*, 5317.
[14] X. Gao, Y. Cui, R. M. Levenson, L. W. K. Chung, S. Nie, *Nat. Biotechnol.* **2004**, *22*, 969.
[15] S. Xiangyang, W. Suhe, M. Sasha, A. Mary, E. Van, B. Xiangdong, L. Inhan, B. James R, Jr, *Small.* **2007**, *3*, 1245
[16] C. M. Spencer, D. Faulds, *Drugs* **1994**, *48*, 794.
[17] M. Ishitobi, E. Shin, N. Kikkawa, *Int. J. Clin. Oncol.* **2001**, *6*, 55.
[18] M. Schmitt-Sody, S. Strieth, S. Krasnici, B. Sauer, B. Schulze, M. Teifel, U. Michaelis, K. Naujoks, M. Dellian, *Clin. Cancer Res.* **2003**, *9*, 2335.
[19] S. D. Gladwin, H. R. R. Gundu, F. W. Robert, C. Thomas, *J. Biomed. Mater. Res.* **2001**, *55*, 96.
[20] Y. Dong, S.-S. Feng, *Biomaterials* **2005**, *26*, 6068.
[21] Z. Liu, X. Sun, N. Nakayama-Ratchford, H. Dai, *ACS Nano* **2007**, *1*, 50.
[22] R. Hergt, S. Dutz, R. Muller, M. Zeisberger, *J. Phys.: Condens. Matter* **2006**, *18*, S2919.
[23] F. Sonvico, S. Mornet, S. Vasseur, C. Dubernet, D. Jaillard, J. Degrouard, J. Hoebeke, E. Duguet, P. Colombo, P. Couvreur, *Bioconjugate Chem.* **2005**, *16*, 1181.
[24] C. C. Berry, A. S. G. Curtis, *J. Phys. D: Appl. Phys.* **2003**, *36*, R198.
[25] S. Mornet, S. Vasseur, F. Grasset, E. Duguet, *J. Mater. Chem.* **2004**, *14*, 2161.
[26] T. Neuberger, B. Schof, H. Hofmann, M. Hofmann, B. von Rechenberg, *J. Magn. Magn. Mater.* **2005**, *293*, 483.
[27] R. Hergt, W. Andra, C. G. d'Ambly, I. Hilger, W. A. Kaiser, U. Richter, H. G. Schmidt, *Magn, IEEE Trans.* **1998**, *34*, 3745.
[28] A. Jordan, R. Scholz, P. Wust, H. Fling, F. Roland, *J. Magn. Magn. Mater.* **1999**, *201*, 413.
[29] P. Wust, B. Hildebrandt, G. Sreenivasa, B. Rau, J. Gellermann, H. Riess, R. Felix, P. M. Schlag, *Lancet Oncol.* **2002**, *3*, 487.
[30] W. Wang, G. K. Liu, H. S. Cho, Y. Guo, D. Shi, J. Lian, R. C. Ewing, *Chem. Phys. Lett.* **2009**, *469*, 149.
[31] C. Laurent, A. Peigney, O. Dumortier, A. Rousset, *J. Eur. Ceram. Soc.* **1998**, *18*, 2005.
[32] A. Peigney, C. Laurent, E. Flahaut, A. Rousset, *Ceram. Int.* **2000**, *26*, 677.
[33] E. Flahaut, A. Peigney, C. Laurent, C. Marliere, F. Chastel, A. Rousset, *Acta Mater.* **2000**, *48*, 3803.
[34] H. Cho, D. Shi, Y. Guo, J. Lian, Z. Ren, B. Poudel, Y. Song, J. L. Abot, D. Singh, J. Routbort, L. Wang, R. C. Ewing, *J. Appl. Phys.* **2008**, *104*, 074302.
[35] Y. Guo, H. Cho, D. Shi, J. Lian, Y. Song, J. Abot, B. Poudel, Z. Ren, L. Wang, R. C. Ewing, *Appl. Phys. Lett.* **2007**, *91*, 261903.
[36] D. Shi, J. Lian, H. Peng, W. Weng, Z. Dong, L. M. Wang, R. C. Ewing, *Adv. Mater.* **2006**, *18*, 189.
[37] F. Wang, G. Dukovic, L. E. Brus, T. F. Heinz, *Science* **2005**, *308*, 838.
[38] J. H. Hodak, A. Henglein, G. V. Hartland, *J. Chem. Phys.* **2000**, *112*, 5942.
[39] K. S. Hong, R. S. Meltzer, B. Bihari, D. K. Williams, B. M. Tissue, *J. Lumin.* **1998**, *76–77*, 234.
[40] B. M. Tissue, *Chem. Mater.* **1998**, *10*, 2837.
[41] R. S. Meltzer, S. P. Feofilov, B. Tissue, H. B. Yuan, *Phys. Rev. B* **1999**, *60*, R14012.
[42] A. P. Bartko, L. A. Peyser, R. M. Dickson, A. Mehta, T. Thundat, R. Bhargava, M. D. Barnes, *Chem. Phys. Lett.* **2002**, *358*, 459.
[43] R. S. Meltzer, K. S. Hong, *Phys. Rev. B* **2000**, *61*, 3396.
[44] G. K. Liu, H. Z. Zhuang, X. Y. Chen, *Nano Lett.* **2002**, *2*, 535.
[45] X. Y. Chen, G. K. Liu, *J. Solid State Chem.* **2005**, *178*, 419.
[46] R. P. Rao, *J. Electrochem. Soc.* **1996**, *143*, 189.
[47] R. P. Rao, *Solid State Commun.* **1996**, *99*, 439.
[48] S. Lanone, F. Rogerieux, J. Geys, A. Dupont, E. Maillot-Marechal, J. Boczkowski, G. Lacroix, P. Hoet, *Part. Fibre Toxicol.* **2009**, *6*, 14.

[49] L. K. Limbach, P. Wick, P. Manser, R. N. Grass, A. Bruinink, W. J. Stark, *Environ. Sci. Technol.* **2007**, *41*, 4158.
[50] S. Park, Y. K. Lee, M. Jung, K. H. Kim, N. Chung, E. K. Ahn, Y. Lim, K. H. Lee, *Inhalation Toxicol.* **2007**, *19*, 59.
[51] K. F. Soto, A. Carrasco, T. G. Powell, L. E. Murr, K. M. Garza, *Mater. Sci. Eng., C* **2006**, *26*, 1421.
[52] F. Tian, D. Cui, H. Schwarz, G. G. Estrada, H. Kobayashi, *Toxicol. in Vitro* **2006**, *20*, 1202.
[53] I. Papageorgiou, C. Brown, R. Schins, S. Singh, R. Newson, S. Davis, J. Fisher, E. Ingham, C. P. Case, *Biomaterials* **2007**, *28*, 2946.
[54] L. L. Hench, J. Wilson, *Science* **1984**, *226*, 630.
[55] M. A. Rauschmann, T. A. Wiechelhaus, V. Stirnal, E. Dingeldein, L. Zichner, R. Schnettler, V. Alt, *Biomaterials* **2005**, *26*, 2667.
[56] A. Bishop, C. Balázsi, J. H. C. Yang, P. I. Gouma, *Polym. Adv. Technol.* **2006**, *17*, 902.
[57] D. Shi, G. Jiang, X. J. Wen, *Appl. Biomater.* **2000**, *53*, 457.
[58] M. Jarcho, *Clin. Orthop. Relat. Res.* **1981**, *157*, 2592.
[59] K. Prabakaran, S. Kannan, S. Rajeswari, *Trends Biomater. Artif. Organs* **2005**, *18*, 2.
[60] K. A. Khor, P. Cheang, *J. Therm. Spray Technol.* **1994**, *3*, 45.
[61] W. F. Hench, *J. Am. Ceram. Soc.* **1991**, *74*, 1487.
[62] M. Hamadouche, L. Sedel, *J. Bone Joint Surg.* **2000**, *82-B*, 1095.
[63] P. Cherukuri, C. J. Gannon, T. K. Leeuw, H. K. Schmidt, R. E. Smalley, S. A. Curley, R. B. Weisman, *PNAS* **2006**, *103*, 18882.
[64] Z. Liu, W. Cai, L. He, N. Nakayama, K. Chen, X. Sun, X. Chen, H. Dai, *Nat. Nanotechnol.* **2006**, *10*, 1038.
[65] X. Y. Chen, L. Yang, R. E. Cook, S. Skanthakumar, D. Shi, G. K. Liu, *Nanotechnology* **2003**, *14*, 670.
[66] V. Väisänen, H. Härmä, H. Lilja, A. Bjartell, *Luminescence* **2000**, *15*, 389.
[67] B. N. G. Giepmans, S. R. Adams, M. H. Ellisman, R. Y. Tsien, *Science* **2006**, *312*, 217.
[68] D. E. Johnson, H.-w. Ai, P. Wong, J. D. Young, R. E. Campbell, J. R. Casey, *J. Biol. Chem.* **2009**, *284*, 20499.
[69] J. C. Waters, *J. Cell Biol.* **2009**, *185*, 1135.
[70] C. Deng, X. Xiong, A. N. Krutchinsky, *Mol. Cell. Proteomics* **2009**, *8*, 1413.
[71] A. Serrels, P. Timpson, M. Canel, J. P. Schwarz, N. O. Carragher, M. C. Frame, V. G. Brunton, K. I. Anderson, *Cancer Res.* **2009**, *69*, 2714.
[72] S. Na, F. Chowdhury, B. Tay, M. Ouyang, M. Gregor, Y. Wang, G. Wiche, N. Wang, *Am. J. Physiol. Cell Physiol.* **2009**, *296*, C868.
[73] L. Brus, *Appl. Phys. A* **1991**, *53*, 465.
[74] A. P. Alivisatos, *J. Phys. Chem.* **1996**, *100*, 13226.
[75] S. Banerjee, S. S. Wong, *Nano Lett.* **2002**, *2*, 195.
[76] J. M. Haremza, M. A. Hahn, T. T. Krauss, *Nano Lett.* **2002**, *2*, 1253.
[77] W. C. Chan, S. M. Nie, *Science* **1998**, *281*, 2016.
[78] M. Bruchez, M. Moronne, Jr, P. Gin, S. Weiss, A. P. Alivisatos, *Science* **1998**, *281*, 2013.
[79] S. J. Rosenthal, I. Tomlinson, E. M. Adkins, S. Schroeter, S. Adams, L. Swafford, J. McBride, Y. Wang, L. G. DeFelice, R. D. Blakely, *J. Am. Chem. Soc.* **2002**, *124*, 4586.
[80] B. Dubertret, P. Skourides, D. J. Norris, V. Noireaux, A. H. Brivanlou, A. Libchaber, *Science* **2002**, *298*, 1759.
[81] J. K. Jaiswal, H. Mattoussi, J. M. Mauro, S. M. Simon, *Nat. Biotechnol.* **2002**, *21*, 47.
[82] P. W. Barone, S. Baik, D. A. Heller, M. S. Strano, *Nat. Mater.* **2004**, *4*, 86.
[83] S. Wray, M. Cope, D. T. Delpy, *Biochem. Biophys. Acta* **1988**, *933*, 184.
[84] L. J. McCartney, J. C. Pickup, O. J. Rolinski, D. J. S. Birch, *Anal. Biochem.* **2001**, *292*, 216.
[85] N. Klonis, N. H. Quazi, L. W. Deady, A. B. Hughes, L. Tilley, *Anal. Biochem.* **2003**, *317*, 47.
[86] S. Kim, Y. T. Lim, E. G. Soltesz, A. M. De Grand, J. Lee, A. Nakayama, J. A. Parker, T. Mihaljevic, R. G. Laurence, D. M. Dor, L. H. Cohn, M. G. Bawendi, J. V. Frangioni, *Nat. Biotechnol.* **2004**, *22*, 93.
[87] J. V. Frangioni, *Curr. Opin. Chem. Bio.* **2003**, *7*, 626.
[88] W. Wang, D. Shi, J. Lian, Y. Guo, G. K. Liu, L. M. Wang, R. C. Ewing, *Appl. Phys. Lett.* **2006**, *89*, 183106.
[89] Y. Guo, D. Shi, J. Lian, Z. Dong, W. Wang, H. Cho, G. Liu, L. Wang, R. C. Ewing, *Nanotechnology* **2008**, *19*, 175102.
[90] M. E. Akerman, W. C. W. Chan, P. Laakkonen, S. N. Bhatia, E. Ruoslahti, *PNAS* **2002**, *99*, 12617.
[91] I. Brigger, C. Dubernet, P. Couvreur, *Adv. Drug Deliv. Rev.* **2002**, *54*, 631.
[92] B. Ballou, B. C. Lagerholm, L. A. Ernst, M. P. Bruchez, A. S. Waggoner, *Bioconjugate Chem.* **2004**, *15*, 79.
[93] G. Jia, H. Wang, L. Yan, X. Wang, T. Yan, Y. Zhao, X. Guo, *Environ. Sci. Technol.* **2005**, *39*, 1378.
[94] C. W. Lam, J. T. James, R. McCluskey, R. L. Hunter, *Toxicol. Sci.* **2004**, *77*, 126.
[95] A. M. Derfus, W. C. W. Chan, S. N. Bhatia, *Nano Lett.* **2004**, *4*, 11.
[96] J. K. Jaiswal, H. Mattoussi, J. M. Mauro, S. M. Simon, *Nat. Biotechnol.* **2003**, *21*, 47.
[97] W. J. Parak, R. Boudreau, M. Le Gros, D. Gerion, D. Zanchet, C. M. Micheel, S. C. Williams, A. P. Alivisatos, C. Larabell, *Adv. Mater.* **2002**, *14*, 882.
[98] D. R. Larson, W. R. Zipfel, R. M. Williams, S. W. Clark, M. P. Bruchez, F. W. Wise, W. W. Webb, *Science* **2003**, *300*, 1434.
[99] A. Hoshino, K. Hanaki, K. Suzuki, K. Yamamoto, *Biochem. Biophys. Res. Commun.* **2004**, *314*, 46.
[100] D. Shi, P. He, J. Lian, L. M. Wang, D. Mast, M. Schulz, *Appl. Phys. Lett.* **2002**, *81*, 5216.
[101] D. Shi, S. X. Wang, W. J. van Ooij, L. M. Wang, J. G. Zhao, Z. Yu, *Appl. Phys. Lett.* **2001**, *78*, 1243.
[102] D. Shi, P. He, J. Lian, L. M. Wang, D. Mast, M. Schulz, *Appl. Phys. Lett.* **2003**, *83*, 5301.
[103] D. Shi, P. He, J. Lian, L. M. Wang, W. J. Van Ooij, *J. Mater. Res.* **2002**, *17*, 981.
[104] Q. L. Fan, K. G. Neoh, E. T. Kang, B. Shuter, S. C. Wang, *Biomaterials* **2007**, *28*, 5426.
[105] H. Iida, K. Takayanagi, T. Nakanishi, T. Osaka, *J. Colloid Interface Sci.* **2007**, *314*, 274.
[106] T. Hyeon, S. S. Lee, J. Park, Y. Chung, H. B. Na, *J. Am. Chem. Soc.* **2001**, *123*, 12798.
[107] H. Xu, L. L. Cai, N. H. Tong, H. Gu, *J. Am. Chem. Soc.* **2006**, *128*, 15582.
[108] J. Cheng, B. A. Teply, I. Sherifi, J. Sung, G. Luther, F. X. Gu, E. Levy-Nissenbaum, A. F. Radovic-Moreno, R. Langer, O. C. Farokhzad, *Biomaterials* **2007**, *28*, 869.
[109] M. Khossravi, Y. H. Kao, R. J. Mrsny, T. D. Sweeney, *Pharm. Res.* **2002**, *19*, 634.
[110] G. T. Hermanson, *Bioconjugate Techniques* **1996**, 8.
[111] D. Sutton, N. Nasongkla, E. Blanco, J. Gao, *Pharm. Res.* **2007**, *24*, 1029.
[112] A. Rosler, G. W. M. Vandermeulen, H. Klok, *Adv. Drug Delivery Rev.* **2001**, *53*, 95.
[113] N. Nishiyama, K. Kataoka, *Pharm. Ther.* **2006**, *112*, 630.
[114] H. Wang, X. Wang, M. A. Winnik, I. Manners, *J. Am. Chem. Soc.* **2008**, *130*, 12921.
[115] P. Bhargava, Y. Tu, J. X. Zhang, H. Xiong, R. P. Quirk, S. Z. D. Cheng, *J. Am. Chem. Soc.* **2007**, *129*, 1113.
[116] D. Chen, H. Peng, M. Jiang, *Macromolecules* **2003**, *36*, 2576.
[117] H. Peng, D. Chen, M. Jiang, *Macromolecules* **2005**, *38*, 3550.
[118] H. Peng, D. Chen, M. Jiang, *J. Phys. Chem. B* **2003**, *107*, 12461.
[119] H. Peng, Y. Lu, *Langmuir* **2006**, *22*, 5525.
[120] L. M. Weiner, G. P. Adams, *Oncogene* **2000**, *19*, 6144.
[121] H. Peng, *J. Phys. Chem. B* **2007**, *111*, 8885.
[122] E. G. Bellomo, M. D. Wyrsta, L. Pakstis, D. J. Pochan, T. J. Deming, *Nat. Mater.* **2004**, *3*, 244.
[123] K. S. Soppimath, D. C. Tan, Y. Yang, *Adv. Mater.* **2005**, *17*, 318.
[124] E. Soussan, S. Cassel, M. Blanzat, I. Rico-Latles, *Angew. Chem, Int. Ed.* **2009**, *48*, 274.

[125] C. J. F. Rijcken, O. Soga, W. E. Hennic, C. F. van Nostrum, *J. Controlled Release* **2007**, *120*, 131.
[126] J. H. Park, G. von Maltzahn, E. Ruoslahti, S. N. Bhatia, M. J. Sailor, *Angew. Chem.* **2008**, *47*, 7284.
[127] R. Weissleder, *Nat. Rev. Cancer* **2002**, *2*, 11.
[128] D. Shi, H. S. Cho, Y. Chen, H. Xu, H. Gu, J. Lian, W. Wang, G. Liu, C. Huth, L. Wang, R. C. Ewing, S. Budko, G. M. Pauletti, Z. Dong, *Adv. Mater.* **2009**, *21*, 2170.
[129] X. M. Wang, H. C. Gu, Z. Q. Yang, *J. Magn. Magn. Mater.* **2005**, *293*, 334.
[130] D. Shi, J. Lian, H. Peng, W. Wang, Z. Dong, L. M. Wang, R. C. Ewing, *Adv. Funct. Mater.* **2008**, *18*, 2489.
[131] D. Shi, Y. Guo, Z. Dong, J. Lian, W. Wang, G. Liu, L. Wang, R. C. Ewing, *Adv. Mater.* **2007**, *19*, 4033.
[132] C. M. Spencer, D. Faulds, *Drugs* **1994**, *48*, 794.
[133] M. Ishitobi, E. Shin, N. Kikkawa, *Int. J. Clin. Oncol.* **2001**, *6*, 55.
[134] L. Mu, S. S. Feng, *J. Controlled Release* **2002**, *80*, 129.
[135] G. R. Das, G. H. R. Rao, R. F. Wilsion, T. Chandy, *J. Biomed. Mater. Res.* **2001**, *55*, 96.
[136] Y. Dong, S. S. Feng, *Biomaterials* **2005**, *26*, 6068.
[137] L. Mu, P. H. Seow, *Colloids Surf, B* **2006**, *47*, 90.
[138] M. N. Moore, *Environ. Int.* **2006**, *32*, 967.
[139] C. M. Sayes, F. Liang, J. L. Hudson, J. Mendez, W. Guo, J. M. Beach, V. C. Moore, C. D. Doyle, J. L. West, W. E. Billups, K. D. Ausman, V. L. Colvin, *Toxicol. Lett.* **2006**, *161*, 135.
[140] M. L. Schipper, N. Nakayama-Ratchford, C. R. Davis, N. Wong, S. Kam, P. Chu, Z. Liu, X. Sun, H. Dai, S. S. Gambhir, *Nat. Nanotechnol.* **2008**, *3*, 216.
[141] T. E. McKnight, A. V. Melechko, G. D. Griffin, M. A. Guillorn, V. I. Merkulov, F. Serna, D. K. Hensley, M. J. Doktycz, D. H. Lowndes, M. L. Simpson, *Nanotechnology* **2003**, *14*, 551.
[142] G. Hashiguchi, T. Goda, M. Hosogi, K. Hirano, N. Kaji, Y. Baba, K. Kakushima, H. Fujita, *Anal. Chem.* **2003**, *75*, 4347.
[143] P. Guo, *J. Nanosci. Nanotechnol.* **2005**, *5*, 1964.
[144] V. Labhasetwar, *Curr. Opin. Biotechnol.* **2005**, *16*, 674.
[145] M. N. Kumar, S. S. Mohapatra, X. Kong, P. K. Jena, U. Bakaowsky, C. M. Lehr, *J. Nanosci. Nanotechnol.* **2004**, *8*, 990.
[146] S. S. Davis, *Trends Biotechnol.* **1997**, *15*, 217.
[147] G. F. Paciotti, L. Myer, D. Weireich, D. Goia, N. Pavel, R. E. McLaughlin, L. Tamarkin, *Drug Delivery* **2004**, *11*, 169.
[148] H. Xu, F. Yan, E. E. Monson, R. Koppelman, *J. Biomed. Mater. Res, Part B: Appl. Biomater.* **2003**, *66A*, 870.